ICARUS

International Journal of Solar System Studies

Published in Affiliation with the Division for Planetary
Sciences, American Astronomical Society

Structural stability of rubble-pile asteroids

Ishan Sharma *

Department of Mechanical Engineering, IIT Kanpur, Kanpur 208 016, India
Mechanics & Applied Mathematics Group, IIT Kanpur, Kanpur 208 016, India

ARTICLE INFO

ABSTRACT

Granular aggregates, like fluids, do not admit all manners of shapes and rotation rates. It is hoped that an analysis of a suspected granular asteroid's equilibrium shape and its structural stability will help confirm its rubble-pile nature, and, perhaps, even constrain the asteroid's material parameters. Equilibrium shapes have been analyzed in the past by several investigators (Holsapple, K.A. [2001]. Icarus 154, 432–448; Harris, A.W., Fahnestock, E.G., Pravec, P. [2009]. Icarus 199, 310–318; Sharma, I., Jenkins, J.T., Burns, J.A. [2009]. Icarus 200, 304–322). Here, we extend the classical Lagrange–Dirichlet stability theorem to the case of self-gravitating granular aggregates. This stability test is then applied to probe the stability of several near-Earth asteroids, and explore the influence of material parameters such as internal friction angle and plastic bulk modulus. Finally, we consider their structural stability to close planetary encounters. We find that it is possible for asteroids to be stable to small perturbations, but unstable to strong and/or extended perturbations as experienced during close flybys. Conversely, assuming stability in certain situations, it is possible to estimate material properties of some asteroids like, for example, 1943 Anteros.

1. Introduction

We are interested in testing the structural stability of freely-rotating rubble-pile asteroids. The equilibrium shapes of these objects have been analyzed previously by Holsapple (2001) via limit analysis, by Harris et al. (2009) who bound the surface's maximum slope by the local angle of repose, and by Sharma et al. (2009) utilizing volume-averaging. At the same time, Richardson et al. (2005) explored the equilibrium shapes of a collective of same-sized smooth rigid spheres via a hard-particle discrete-element simulation, while more recently Sanchez and Scheeres (2011, 2012) have utilized soft-particle discrete element simulations to investigate the equilibria and dynamics of granular aggregates in space.

Much work is available in the stability of rotating fluid ellipsoids subjected to gravitational and tidal forces; see, e.g., Chandrasekhar (1969), Jeans (1961) and Lyttleton (1953). In contrast, except for the recent work of Holsapple (2004), the stability of spinning ellipsoidal granular aggregates has not been explored. As we will see, typical stability tests employed for fluids do not carry over in a straightforward manner, if at all, to the case of rubble-piles on account of them being most conveniently modeled as *non-smooth* materials; cf. Section 3. A stability test for rotating non-smooth complex fluids was recently developed by Sharma

(2012), and we extend it to the case of granular aggregates. We will utilize our stability test to investigate several near-Earth asteroids. We also compare our approach with that of Holsapple (2004) at Section 7.3's end. Finally, we extend our analysis of local stability under infinitesimal perturbations to include finite disturbances via an approximate higher-order stability analysis.

In our analysis, we will model rubble-pile asteroids as homogeneous isotropic self-gravitating rigid-plastic ellipsoids, and, furthermore, restrict ourselves to deformations that retain the body's ellipsoidal shape, i.e., *homogeneous deformations*. Sharma et al. (2009), henceforth Paper I, derives relevant dynamical equations. For reasons discussed later, the stability of rotating bodies is best tested from within a rotating coordinate system. Thus, we first re-derive the governing dynamical equations below, separating out the effects of an underlying rotating coordinate system.

2. Homogeneous dynamics in a rotating frame

Sharma (2012), henceforth Paper II, derives equations for a homogeneously deforming ellipsoid in a rotating frame from first principles. Here, for reasons of completeness and continuity, we adapt the derivation of Paper I done in a fixed coordinate system to a rotating frame.

We recall that during homogeneous deformation, the material velocity

$$\overset{\circ}{\mathrm{x}} = \boldsymbol{L}_F \cdot \mathrm{x}, \tag{1}$$

* Address: Department of Mechanical Engineering, Indian Institute of Technology Kanpur, Kanpur 208 016, India.
  E-mail address: ishans@iitk.ac.in

with × locating a material point, $(°)$ denoting the time derivative in a fixed frame[1] and L_F being the motion's velocity gradient that is spatially homogeneous but possibly time-varying; here the subscript 'F' indicates that the velocity gradient is with respect to a fixed frame. Equations governing a homogeneously deforming ellipsoid free from surface forces but experiencing the body force[2] b are (Sharma et al., 2009):

$$\left(\mathring{L}_F + L_F^2\right) \cdot I = -\bar{\sigma}V + M^T, \quad \text{and} \tag{2a}$$

$$\mathring{I} = L_F \cdot I + I \cdot L_F^T, \tag{2b}$$

where $\bar{\sigma}$ is the volume-averaged stress tensor,

$$I = \int_V \rho \times \otimes \times dV, \quad \text{and} \tag{3a}$$

$$M = \int_V \rho \times \otimes b \, dV, \tag{3b}$$

being, respectively, the ellipsoid's inertia tensor and external moment tensor, ρ and V are the ellipsoid's density and volume, respectively, and the *tensor product* $(\otimes)$ for any two vectors a and b is defined in indical notation by $(a \otimes b)_{ij} = a_i b_j$. The first equation above follows L_F's evolution by balancing inertial forces, internal stresses and self-gravitation, while the second describes the changing inertia tensor. The inertia tensor I should be contrasted with Euler's moment of inertia tensor frequently employed in dynamics; cf. (23). Finally, we refer the reader to the Appendix of Sharma (2009) for a short summary of relevant tensor algebra.

We now adapt the above formulae to a coordinate system $\mathcal{O}$ rotating at a possibly time-varying rate $\omega(t)$. It is helpful to introduce the anti-symmetric tensor $\Omega(t)$ that satisfies

$$\omega \times \times = \Omega \cdot \times; \tag{4}$$

thus, ω is Ω's associated *axial vector*. We employ rotation rate vectors, such as ω, and their corresponding *angular-velocity tensors*, like Ω, interchangeably. From, say, Lubarda (1999, p. 41), the rates of change in $\mathcal{O}$ of a vector a and a tensor B may be related to their rates of change in a fixed frame by, respectively,

$$\mathring{a} = \dot{a} + \Omega \cdot a \quad \text{and} \quad \mathring{B} = \dot{B} + \Omega \cdot B - B \cdot \Omega,$$

where now, and henceforth, $(\cdot)$ indicates a time derivative in the rotating frame $\mathcal{O}$. Thus, if $\hat{e}_i$ are unit vectors defining $\mathcal{O}$, then $\dot{a} = \mathring{a}_i \hat{e}_i$ and $\dot{B} = \mathring{B}_{ij} \hat{e}_i \otimes \hat{e}_j$. Viewing the homogeneously deforming ellipsoid from within $\mathcal{O}$, we may now rewrite (1) as

$$v = \dot{x} = L \cdot x, \tag{5}$$

where v is the relative velocity of a material point in $\mathcal{O}$ and

$$L = L_F - \Omega, \tag{6}$$

is the velocity gradient observed in the rotating frame $\mathcal{O}$. Similarly, the set (2) becomes

$$(\dot{L} + L^2) \cdot I = -\bar{\sigma}V + M^T - (\dot{\Omega} + \Omega^2 + 2\Omega \cdot L) \cdot I, \quad \text{and} \tag{7a}$$

$$\dot{I} = L \cdot I + I \cdot L^T. \tag{7b}$$

We note that the stress and moment tensors remain unaffected by rigid body rotation, as does the form for I's rate of change. In the first equation, the bracketed three terms on the right-hand side stem from, respectively, angular, centripetal and Coriolis' accelerations, and act in the rotating frame as external moment tensors. The two equations above follow an ellipsoid's motion as it deforms homogeneously relative to the frame $\mathcal{O}$ according to (5).

The above two equations contain three unknown fields, viz., L, $\bar{\sigma}$ and I. Thus, a closure equation is required. This is provided by

introducing a constitutive law. Given our interest in rubble-pile asteroids, we will next introduce a rheology that describes these granular aggregates.

3. Rheology

In the past, Sharma (2004, 2009, 2010) and Sharma et al. (2005, 2009) have modeled a rubble-pile's constitutive response by that of a rigid perfectly-plastic cohesionless material obeying a Drucker–Prager yield criterion and an appropriate *flow rule* that governed the material's behavior post-yield. Paper I chose for simplicity a *non-associative* flow rule that preserved volume during plastic flow. Here we consider an *associative* flow rule; non-associative rigid-plastic materials are typically trivially *secularly*[3] unstable, as we show in a later section.

We first quickly introduce the Drucker–Prager yield criterion whose smoothness makes it amenable to three-dimensional dynamic problems. To formulate this rule, we define the pressure

$$p = -\frac{1}{3}\text{tr}\sigma, \tag{8}$$

and the deviatoric stress

$$s = \sigma + p\mathbf{1}. \tag{9}$$

The Drucker–Prager condition may now be written as

$$|s|^2 \leqslant k^2 p^2, \tag{10}$$

where $|s|$ is s' magnitude given by

$$|s|^2 = s_{ij} s_{ij},$$

utilizing the summation convention, and

$$k = \frac{2\sqrt{6}\sin\phi_F}{3 - \sin\phi_F}, \tag{11}$$

in terms of the granular aggregate's internal friction angle ϕ_F. Employing the principal stresses σ_i, we have

$$|s| = \frac{1}{3}\{(\sigma_1 - \sigma_2)^2 + (\sigma_2 - \sigma_3)^2 + (\sigma_3 - \sigma_1)^2\}$$
$$= \frac{2}{3}(\tau_1^2 + \tau_2^2 + \tau_3^2), \tag{12}$$

where $\tau_i = (\sigma_j - \sigma_k)/2$, $i \neq j \neq k$ are the principal shear stresses. Therefore, $|s|$ is a measure of the 'total' shear stress, and, consequently, the yield criterion (10) limits the shear stress in terms of the pressure and the internal friction angle. This internal friction models the ability of an aggregate to support shear stresses, and is traced to both the usual *interfacial* friction due to particle interaction, as well as a *geometric* friction due to interlocking and rearrangement of finite-sized constituents. The latter is generally dominant in dense aggregates, but decreases with lowering density. Similarly, ϕ_F is greatly affected by confining pressure, with grain crushing lowering ϕ_F when the confining pressure is 1 MPa or beyond. Typically dense soils at these confining pressures display ϕ_F between 30° and 40°. We discuss soil behavior in more detail in Section 7.1. In passing, it is worth mentioning the alternate Mohr–Coulomb yield criterion wherein relation (10) is phrased in terms of the greatest shear stress rather than $|s|$; see Chen and Han (1988, Section 2.3.3, p. 88). This yield criterion was utilized by Holsapple (2001, 2004). Sharma et al. (2005) and later Sharma et al. (2009) showed that utilizing Drucker–Prager yield surface allowed for a better match with simulations of Richardson et al. (2005). The recent simulations of Sanchez and Scheeres (2012) confirm this latter prediction.

---

[1] We slightly modify Paper I's notation for future convenience.
[2] Force per unit mass.

[3] Systems found stable by the energy criterion are secularly stable, cf. Section 5.2.

Consider next the *flow rule* relating stress and stain increments post-yield. These are traditionally obtained from an assumed *plastic potential g* that defines a surface in stress space that facilitates a relation between stress and strain increments; see, e.g., Chen and Han (1988, Section 4.2, p. 181). Associative flow rules are found by selecting the yield surface as the plastic potential, i.e.,

$$g = |\boldsymbol{s}|^2 - k^2 p^2. \tag{13}$$

To obtain the flow rule, we assume that when the material is stressed beyond yield, the incremental strain $d\varepsilon$ – thought of as a six-dimensional vector – at a stress state is normal to the surface described by g passing through that stress point, i.e.,

$$d\varepsilon_{ij} \sim dg/d\sigma_{ij} = s_{ij} - \frac{k^2}{27}\sigma_{kk}\delta_{ij} = s_{ij} + \epsilon p \delta_{ij},$$

where the equality follows from differentiating formula (13), and $\epsilon = k^2/9$; cf. point 'E' in Fig. 1. Introducing the proportionality constant dq, the above may be written as

$$d\varepsilon = (\boldsymbol{s} + \epsilon p \boldsymbol{1}) dq,$$

which, after converting to an objective rate form, becomes

$$\boldsymbol{D} = (\boldsymbol{s} + \epsilon p \boldsymbol{1})\dot{q}, \tag{14}$$

where the *stretching-rate tensor* $\boldsymbol{D}$ captures the stretching rates and is the symmetric part of the velocity gradient $\boldsymbol{L}$, and $\dot{q}$ is again a constant. A deformation that follows (14) is said to be *compatible*. In flow rule (14), we may employ the stretching-rate tensor as observed in the rotating frame $\mathcal{O}$, as pure rotation leaves the symmetric part of the velocity gradient unaffected; cf. (6).

To obtain $\dot{q}$, we combine (14) with the yield criterion (10) and find

$$\dot{q} = \frac{1}{p\sqrt{k^2 + 3\epsilon^2}}|\boldsymbol{D}|, \tag{15}$$

with $|\boldsymbol{D}|^2 = D_{ij}D_{ij}$. Substituting the above in (14), we obtain the deviatoric stress post-yield in terms of the strain rate:

$$\boldsymbol{s} = p\left(\sqrt{k^2 + 3\epsilon^2}\frac{\boldsymbol{D}}{|\boldsymbol{D}|} - \epsilon\boldsymbol{1}\right), \tag{16}$$

where p is the pressure as defined in (8). Combining the above with (9) yields the complete stress tensor during yielding
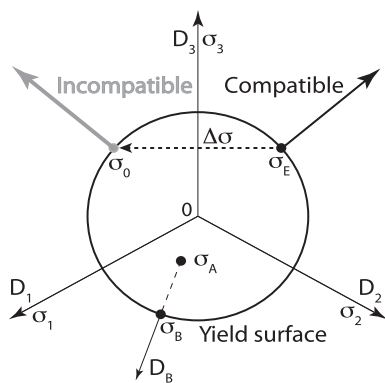

Fig. 1. The Drucker–Prager yield surface in principal-stress/strain space appears as a circle when viewed on a plane perpendicular to the pressure axis $\sigma_1 = \sigma_2 = \sigma_3$. The point '$E$' corresponds to the stress state at equilibrium. The strain rate compatible to the stress state $\boldsymbol{\sigma}_E$ at 'E' is normal to the yield surface there. If the incompatible strain rate shown by the gray vector is superimposed, the stress state immediately shifts to a location $\boldsymbol{\sigma}_0$ on the yield surface where the imposed strain rate would be compatible. This leads to jump $\Delta\boldsymbol{\sigma}$ in the stress state. The stress state $\boldsymbol{\sigma}_A$ is not at yield, but may move to a state $\boldsymbol{\sigma}_B$ on the yield surface with corresponding compatible strain rate $\boldsymbol{D}_B$ under the action of external forces; cf. Section 6.4.

$$\boldsymbol{\sigma} = -p(1+\epsilon)\boldsymbol{1} + p\sqrt{k^2 + 3\epsilon^2}\frac{\boldsymbol{D}}{|\boldsymbol{D}|} \tag{17}$$

that in component form reads

$$\sigma_{ij} = -p(1+\epsilon)\delta_{ij} + p\sqrt{k^2 + 3\epsilon^2}\frac{D_{ij}}{\sqrt{D_{kl}D_{kl}}}.$$

It remains to obtain the pressure p during plastic flow. Taking the trace of (17), we find the *dilatation rate*

$$\mathrm{tr}\boldsymbol{D} = \frac{3\epsilon|\boldsymbol{D}|}{\sqrt{k^2 + 3\epsilon^2}}, \tag{18}$$

where 'tr' denotes a tensor's trace. Because the material dilates post-yield, we need to postulate a relation between the pressure and the dilatation. A simple linear relationship is:

$$\dot{p} = -\kappa\,\mathrm{tr}\boldsymbol{D}, \tag{19}$$

where κ is the granular aggregate's *plastic bulk modulus* post-yield. Because (18) is positive, the material expands after yielding leading to a drop in the pressure. We discuss possible values for aggregates such as sand in detail in Section 7.1. Here, we simply note that for sands confined at hundreds of kilo-Pascals, the bulk modulus is of the order of 1 MPa. In the above constitutive postulate, we could have included a relation between pressure and dilatation rate via a *bulk viscosity*, but because viscosity does not influence either the system's equilibrium or its secular stability, we ignore viscous effects; see, e.g., Ziegler (1968, p. 91). Similarly, non-linear terms in (19) will not affect a local stability analysis.

Here, we consider homogeneous dynamics where the velocity gradient, and, so, the strain rate $\boldsymbol{D}$ is uniform across the body. Consequently, so is the stress field, and the volume-averaged stress field $\bar{\boldsymbol{\sigma}}$ coincides with the actual local stress $\boldsymbol{\sigma}$. We will, therefore, in the sequel employ the constitutive relations (17) and (19) post-yield with $\bar{\boldsymbol{\sigma}}$ and $\bar{p}$ replacing $\boldsymbol{\sigma}$ and p, respectively. Finally, we note that for a homogeneously deforming body, its average density ρ and its volume V change according to

$$\frac{\dot{V}}{V} = -\frac{\dot{\rho}}{\rho} = \mathrm{tr}\boldsymbol{D}. \tag{20}$$

The stress tensor (17) depends on the strain rate through the ratio $\boldsymbol{D}/|\boldsymbol{D}|$, and is reminiscent of dry friction with k and $\bar{p}$ playing the role of a friction coefficient and a normal force, respectively. This should be compared with the rate-dependent constitutive relations frequently employed for rapid granular flows discussed by Jenkins and Zhang (2002).

To summarize, we employ a rigid-perfectly-plastic material with a Drucker–Prager yield surface as a model for our asteroid. The yield criterion is coupled with an associative flow rule to provide stresses during plastic flow. We emphasize that the constitutive model so obtained is *non*-smooth in that the system's response change character abruptly at yield. We next explore how our chosen rheology limits the range of equilibrium shapes in rotating rubble-pile ellipsoids. Throughout we assume the asteroid to be isotropic and homogenous.

4. Equilibrium shapes

An equilibrated rubble-pile asteroid will rotate rigidly as long as the internal stresses do not violate the yield criterion (10). At equilibrium, we align the coordinate frame $\mathcal{O}$ with the ellipsoidal asteroid's principal axes, so that $\boldsymbol{L}$ and its derivative in $\mathcal{O}$ vanish, while $\boldsymbol{\omega}$ equals the asteroid's equilibrium rotation rate ω_E. Furthermore, for an isolated homogeneous ellipsoidal asteroid that is free from tidal interaction, the body force is due only to self-gravity, and Sharma et al. (2009) show that

$$\boldsymbol{M} = -2\pi\rho G\boldsymbol{I} \cdot \boldsymbol{A}, \tag{21}$$

where $\boldsymbol{A}$ is the *self-gravity shape tensor* that captures the dependence of an ellipsoid's internal gravitational field on its axes ratios $\alpha = a_2/a_1$ and $\beta = a_3/a_1$. Relevant formulae for $\boldsymbol{A}$ in the ellipsoid's principal axes are available in Section 2.4 of Paper I. We note that both $\boldsymbol{A}$ and $\boldsymbol{I}$ are diagonalized in the ellipsoid's principal axes system, so that they commute. Employing $\mathcal{O}$'s definition and $\boldsymbol{M}$'s formula above in (7a), the latter reduces at equilibrium to

$$\bar{\boldsymbol{\sigma}}_E V = -\left(2\pi\rho G\boldsymbol{A} + \boldsymbol{\Omega}_E^2\right) \cdot \boldsymbol{I}, \tag{22}$$

which relates the average equilibrium stress $\bar{\boldsymbol{\sigma}}_E$ to internal gravity and centrifugal stresses; recall that $\boldsymbol{\Omega}_E$ and $\boldsymbol{\omega}_E$ are related as per (4). The stress $\bar{\boldsymbol{\sigma}}_E$ is then combined with the yield criterion (10) to establish necessary relations between the asteroid's equilibrated rotation rate and its ellipsoidal shape at equilibrium. In the three-dimensional shape (α, β)–spin (ω_E) space, these conditions delineate regions parameterized by the internal friction angle ϕ_F, and bound, in general, by an *upper* and a *lower critical surface*. A rubble-pile ellipsoid with friction angle *at least* ϕ_F can exist at equilibrium within the region corresponding to that ϕ_F. This three-dimensional landscape is explored by appropriate two-dimensional sections. An example is shown in Fig. 2, where the equilibrium regions in shape–spin space for an oblate $(a_1 = a_2 \geqslant a_3)$ rubble-pile asteroid rotating at ω_E about its shortest axis $\hat{e}_3$ are displayed for several choices of internal friction angle ϕ_F. The classical shapes for inviscid fluids – the *Maclaurin spheroids* – are obtained for $\phi_F = 0°$. Here, and subsequently, we assume that the equilibrated ellipsoidal asteroid rotates about its shortest axis $\hat{e}_3$, i.e., $\boldsymbol{\omega}_E = \omega_E\hat{e}_3$. This is prompted by the knowledge that freely rotating dissipative bodies will ultimately align into pure rotation about their shortest axis; see, e.g., Burns and Safronov (1973) and Sharma et al. (2005).

Fig. 2 confirms that for any fixed ϕ_F there is an *upper* and, often, a *lower critical equilibrium curve* within which the ellipsoidal asteroid may persist at equilibrium. At faster rotation rates, yielding is initiated by large shear stresses that are a consequence of centrifugal stresses dominating self-gravitational stresses. Beyond the $\phi_F = 90°$ curve yielding is caused by the radial stress in the equatorial plane becoming tensile, and we identify this as the *disruption curve*. If the rotation rate becomes too small, self-gravity over-

whelms both the centrifugal stresses and the frictional resistance. Similar equilibrium regions may be located for prolate $(a_1 \geqslant a_2 = a_3)$ and triaxial $(a_1 > a_2 > a_3)$ ellipsoids; see Paper I. We emphasize that the yield criterion puts a lower bound on a rubble-pile asteroid's internal friction angle; an asteroid's location in shape–spin space only precludes friction angles corresponding to the equilibrium zones outside of which it lies.

We now probe the stability of equilibrated rubble-pile ellipsoidal asteroids.

5. Stability

Local stability in the sense of Lyapunov requires that small perturbations of a system lead to small and bounded departures of its coordinates from their equilibrium values; see, e.g., LaSalle and Lefschetz (1961, p. 28). Stability is typically probed via *spectral* methods that require investigating the eigenvalues of the linearized governing equations and, or by *energy* methods that, in conservative systems, tests whether the system's equilibrium lies at the bottom of an appropriately defined energy well; see, e.g., Nguyen (2000, Chapter 6). Depending on which of the two methods is employed a system is said to be, respectively, *spectrally/dynamically* or *energetically/secularly* stable/unstable. Spectral analysis is predicated on the amenability of the system's governing equations to linearization, and the belief that any possible motion of the system may be expanded as a linear combination of the spectral modes employed. The former requirement precludes its application to the current investigation where we have modeled granular aggregates via a non-smooth constitutive law. We will, therefore, employ an incremental version of the energy criterion to test stability of our system.

We note that for finite dimensional systems (a) secular stability is equivalent to Lyapunov stability, and (b) secularly stable systems are dynamically stable, but the converse is not always true as *gyroscopic* forces may stabilize energetically unstable systems; cf. Section 5.2. These statements may not hold for infinite dimensional continuous systems, and we refer the interested reader to Paper II and references therein. Here, we will restrict ourselves to homogeneous deformations that constitute a finite-dimensional system.

Before formulating the energy criterion, we discuss the coordinate system's role in stability analyses.

5.1. Coordinate system

As Paper II discusses via various examples, the choice of coordinate system is critical to obtain a physically relevant stability prediction. Systems observed in one coordinate system to remain in the vicinity of their equilibrium states may well diverge when viewed from another. For example, a rotating rigid body is stationary, and, hence, trivially stable to an observer who rotates with the body, but is unstable when viewed from a fixed system; rotation takes material points far away from their initial locations. For rotating deformable bodies the situation is more complicated, as the body's changing shape may cause its average rotation to change in order to conserve angular momentum. This was pointed out first by Schwarzschild in 1897 in the context of spinning gas clouds; see the discussion in Jeans (1961, p. 199). Another example are the Jacobi ellipsoids that are the truly triaxial ellipsoidal equilibrium shapes of rotating inviscid fluids. As Jeans (1961) and Lyttleton (1953) indicate, the Jacobi ellipsoids are secularly *unstable* to homogeneous perturbations when viewed from within a coordinate system that rotates steadily at the ellipsoid's equilibrium rotation rate, but are secularly stable when observed from a coordinate system that rotates so as to keep the relative angular momentum of the deforming body zero.
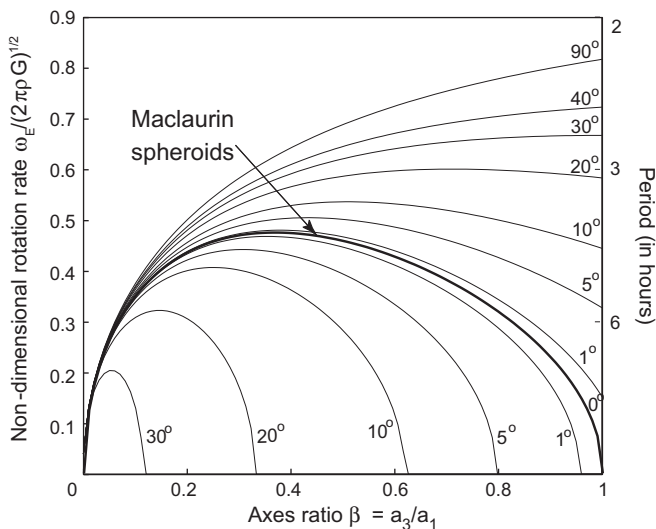
Fig. 2. Regions in shape (β)–spin (ω_E) space where an oblate ellipsoidal asteroid with $\alpha = 1$ can exist in equilibrium. Numbers next to the curves indicate the corresponding friction angle ϕ_F. For a particular ϕ_F, a range of shapes are possible for rotation rates faster ($|\sigma_3|$ is maximum stress) or slower ($|\sigma_3|$ is minimum stress) than that of a Maclaurin spheroid. This plot follows Fig. 3 in Paper I.

Paper II rigorously develops the coordinate system $\mathcal{O}$'s description that appears most appropriate to discuss the stability of rotating deformable bodies. This happens to be the *Tisserand's mean axis of the body*; see, e.g., Munk and MacDonald (1960, p. 10), that minimize the difference $\int_V |u - \omega \times x|^2 \, dV$ between a material point's actual velocity u and the velocity that it would have were the body rotating rigidly with the frame $\mathcal{O}$. Furthermore, it may be shown that the body's relative angular momentum as measured in $\mathcal{O}$,

$$H_{rel} = \int_V x \times \rho v \, dV,$$

vanishes. The Tisserand's mean axis of the body, thus, best isolate the average rigid body rotation embedded in a deformable body's motion.

Given the above choice of coordinate frame $\mathcal{O}$, we need to follow $\mathcal{O}$'s rotation rate's evolution $\dot{\omega}$ post-perturbation. This is complicated for general perturbations, and we refer the interested reader to Paper II. Here, we restrict ourselves to situations wherein the body continues post-perturbation to rotate about a principal axis of inertia. We first note that the body's total angular momentum may be split as

$$H = H_{rel} + \boldsymbol{J} \cdot \boldsymbol{\omega},$$

where

$$\boldsymbol{J} = \operatorname{tr} \boldsymbol{I} - \boldsymbol{I}, \tag{23}$$

is the *Euler's moment of inertia tensor*. Differentiating H, noting that $\dot{H} = 0$ because external torques are absent and H is along a principal axis, and also recalling that $\dot{H}_{rel} = 0$ by $\mathcal{O}$'s definition, we obtain

$$\dot{\boldsymbol{\omega}} = -\boldsymbol{J}^{-1} \cdot \dot{\boldsymbol{J}} \cdot \boldsymbol{\omega}. \tag{24}$$

For homogeneous motions, $\dot{\boldsymbol{J}}$ is obtained by differentiating (23) and employing (7b). Finally, there is the possibility that $\mathcal{O}$'s rotation rate may suddenly change from just before the perturbation to just after, unless the perturbations introduce *no* angular momentum. Paper II discusses this in detail.

To summarize, we will investigate the stability of rubble-pile asteroids from within a coordinate system $\mathcal{O}$ that rotates in order to keep the relative angular momentum of the body zero. We now develop the energy criterion for stability.

5.2. Energy criterion

Following Pearson (1955), we adopt the following definition of secular stability:

A system's equilibrium state is <u>stable</u> *if during a virtual displacement the work done on the system by external agencies is less than the total energy stored and/or dissipated by the system.*

This statement of the energy criterion utilizes the concept of a *virtual displacement* that is the difference between the locations of the system's equilibrium and any other *kinematically admissible* configuration. Configurations and motions that do not violate any kinematic constraints imposed on the system are termed kinematically admissible. Traditionally, virtual displacements are thought of as kinematically admissible motions that occur over zero time. This is sufficient for systems that are describable in terms of potentials, so that the system's response is path independent. However, this is not so in the present case, as plastic dissipation is strongly path dependent. In the past, authors such as Hill (1957) circumvented this issue by introducing a time-like variable to facilitate integration along a virtual displacement following an initial perturbation. Changes in the system's constraints and applied external force fields were included in the integration. This process, however, leaves no distinction between virtual displacements and

kinematically admissible motions that would ensue if the system evolved dynamically from prescribed initial conditions. Given this, we recast the above stability test as:

A system's equilibrium state is <u>stable</u> *if during a kinematically permissible infinitesimal displacement the work done on the system by external agencies is less than the total energy stored and/or dissipated by the system.*

These kinematically permissible infinitesimal displacements may be obtained, for example, by superimposing a *kinematically admissible velocity field* on the body and following the body's motion for an infinitesimal length of time. By doing so we will below rephrase the stability criterion in terms of kinematically admissible velocity fields. The energy criterion as stated is an appropriately modified version of the classical *Lagrange–Dirichlet stability theorem* suitable for dissipative systems governed by possibly non-smooth constitutive laws. The Lagrange–Dirichlet theorem is exclusively applicable to conservative smooth dynamical systems; see, e.g., Nguyen (2000, p. 97).

Pearson's (1955) definition of stability was adopted by Hill (1957), Chakrabarty (1969) and Storåkers (1977) in their investigations into the stability of rigid-plastic materials. A general form suitable for rotating non-smooth complex fluids, of which rubble-pile asteroids are an example, was derived recently by Paper II, who then specialized it for homogeneously deforming bodies. For the sake of clarity, continuity and completeness, we obtain below via an alternative route an abridged version of the energy criterion suitable for our purposes.

As stated, the energy criterion above is applicable for systems that are stationary at equilibrium. We may easily adapt it to rotating systems by an application of D'Alembert's principle (Greenwood, 1988, p. 23). This is equivalent to rewriting the linear momentum balance in the rotating frame $\mathcal{O}$:

$$\nabla \cdot \boldsymbol{\sigma} + \rho(b - \dot{\boldsymbol{\Omega}} \cdot x - \boldsymbol{\Omega}^2 \cdot x - 2\boldsymbol{\Omega} \cdot v) = \rho \dot{v}, \tag{25}$$

where $\dot{\boldsymbol{\Omega}} \cdot x = \dot{\boldsymbol{\omega}} \times x$, $\boldsymbol{\Omega}^2 \cdot x = \boldsymbol{\omega} \times (\boldsymbol{\omega} \times x)$ and $2\boldsymbol{\Omega} \cdot v = 2\boldsymbol{\omega} \times v$ are, respectively, the inertial, centripetal and Coriolis accelerations, and we recall that $\dot{v} = \dot{\mathring{v}}_i \hat{e}_i$ is the material point's relative acceleration observed in $\mathcal{O}$.

We will investigate stability by providing the material points of the equilibrated body by an initial velocity perturbation. In general, if perturbations are allowed to change the body's relative angular momentum, $\mathcal{O}$'s rotation rate will change abruptly across a perturbation. In that case we have to distinguish between the velocity perturbation observed in $\mathcal{O}$ just before, and just after, the perturbation. Paper II discusses this in greater detail, and further shows that if we allow perturbations to introduce angular momentum, then it is always possible to find a perturbation that will render the body locally secularly unstable.[4] Thus, henceforth, we will assume that perturbations do *not* add any angular momentum, so that $\mathcal{O}$'s rotation rate remains unaffected.

Now, let the equilibrated body be perturbed at $t = 0$ by a velocity field $v(x,0) = v_0(x)$ *relative* to the rotating frame $\mathcal{O}$. Post-perturbation, over the small time δt, these material points will displace by $\int_0^{\delta t} v \, dt$. The work done in the rotating frame $\mathcal{O}$ by external agencies during δt is

$$\delta W = \int_0^{\delta t} \int_{V(t)} \rho(b - \dot{\boldsymbol{\Omega}} \cdot x - \boldsymbol{\Omega}^2 \cdot x) \cdot v \, dV \, dt,$$

---

[4] This result, though mathematically correct, appears physically unreasonable. It is necessary, therefore, to modify the current approach to meaningfully include perturbations that change angular momentum. Past works generally ignored angular momentum perturbations, and when not, arrived at the same conclusion as here.

as the Coriolis force does not do any work, and we ignore surface forces in the context of asteroids. The Coriolis force is a gyroscopic force that may dynamically stabilize systems predicted to be secularly unstable. The energy stored/dissipated over δt is obtained by integrating the *stress power* per unit volume over the body's volume and time δt (Holzapfel, 2001, p. 153):

$$\delta E = \int_0^{\delta t} \int_{V(t)} \boldsymbol{\sigma} : \boldsymbol{L} \, dV \, dt,$$

where for two tensors $\boldsymbol{A}$ and $\boldsymbol{B}$, $\boldsymbol{A}:\boldsymbol{B} = A_{ij}B_{ji}$. Everywhere above the spatial integration is over the body's current volume $V(t)$ that changes as the body deforms due to the initial perturbation. The energy criterion ensures secular stability if

$$\delta E > \delta W.$$

We now obtain an alternative form. Taking the dot product of (25) with v and integrating over the body's volume and time δt, and comparing with formulae derived for δE and δW, we find that

$$\delta W - \delta E = \delta E_k,$$

where E_k is the *relative kinetic energy* measured in the rotating frame $\mathcal{O}$:

$$E_k = \int_{V(t)} \frac{1}{2} \rho v \cdot v \, dV, \tag{26}$$

and δE_k is E_k's change over time δt. The energy criterion now requires that for stability the kinetic energy relative to $\mathcal{O}$ decreases over δt, i.e.,

$$\delta E_k < 0. \tag{27}$$

Probing the above inequality is not easy for general motions, and we will restrict ourselves to test the stability of bodies that deform homogeneously according to (5). Thus, the initial velocity perturbation is also homogeneous:

$$v(x, 0) = v_0(x) = \boldsymbol{D}_o \cdot x, \tag{28}$$

where $\boldsymbol{D}_o$ is a symmetric tensor. The initial perturbations, thus, do not add any rigid body rotation. Nevertheless, the above velocity field will in general introduce angular momentum, and thereby cause $\mathcal{O}$'s rotation rate to change abruptly, unless $\boldsymbol{D}_o$ is further restricted to having no shearing action when viewed in the ellipsoid's principal axes frame; in which case $\boldsymbol{I}$ and $\boldsymbol{D}_o$ will commute.

Introducing (5) for v into E_k's definition (26), and employing (3a) provides

$$E_k = \frac{1}{2} \int_V \rho(\boldsymbol{L} \cdot x) \cdot (\boldsymbol{L} \cdot x) \, dV = \frac{1}{2} \boldsymbol{L} \cdot \boldsymbol{I} : \boldsymbol{L}^T.$$

Now, $\delta E_k = \int_0^{\delta t} \dot{E}_k \, dt$. Differentiating the above expression, we obtain

$$\dot{E}_k = \frac{1}{2} (\dot{\boldsymbol{L}} \cdot \boldsymbol{I} : \boldsymbol{L}^T + \boldsymbol{L} \cdot \dot{\boldsymbol{I}} : \boldsymbol{L}^T + \boldsymbol{L} \cdot \boldsymbol{I} : \dot{\boldsymbol{L}}^T).$$

Replacing $\dot{\boldsymbol{L}}$ and $\dot{\boldsymbol{I}}$ from (7a) and (7b), respectively, and simplifying, we obtain

$$\dot{E}_k = \left\{ -\bar{\boldsymbol{\sigma}}V + \boldsymbol{M}^T - (\dot{\boldsymbol{\Omega}} + \boldsymbol{\Omega}^2) \cdot \boldsymbol{I} \right\} : \boldsymbol{L}^T,$$

where we have utilized the fact that $\boldsymbol{\Omega} \cdot \boldsymbol{L} \cdot \boldsymbol{I} : \boldsymbol{L}^T = 0$, which is a reflection of the fact that Coriolis' force does not do any work. Thus, finally,

$$\delta E_k = \int_0^{\delta t} \left\{ -\bar{\boldsymbol{\sigma}}V + \boldsymbol{M}^T - (\dot{\boldsymbol{\Omega}} + \boldsymbol{\Omega}^2) \cdot \boldsymbol{I} \right\} : \boldsymbol{L}^T \, dt. \tag{29}$$

Further progress is possible within the constraints of a local stability analysis, wherein a material point's displacement $\int_0^{\delta t} v \, dt$ following the velocity perturbation v_0 is small. This is equivalent

to requiring that δt is small, allowing us to expand δE_k about $t = 0^+$, i.e., the instant after v_0 is imposed, as

$$\delta E_k = \delta^{(1)} E_k \delta t + \delta^{(2)} E_k \frac{\delta t^2}{2} + O(\delta t^3),$$

where

$$\delta^{(1)} E_k = \left\{ -\bar{\boldsymbol{\sigma}}_0 V + \boldsymbol{M}_0^T - \boldsymbol{\Omega}_E^2 \cdot \boldsymbol{I} \right\} : \boldsymbol{D}_o, \quad \text{and} \tag{30a}$$

$$\delta^{(2)} E_k = \frac{d}{dt} [\{ -\bar{\boldsymbol{\sigma}}V + \boldsymbol{M}^T - (\dot{\boldsymbol{\Omega}} + \boldsymbol{\Omega}^2) \cdot \boldsymbol{I} \} : \boldsymbol{L}^T]\big|_0, \tag{30b}$$

where the subscript '0' indicates evaluation at $t = 0^+$ and we have recognized that $\boldsymbol{L}_0 = \boldsymbol{D}_o$ and $\boldsymbol{\Omega}_0 = \boldsymbol{\Omega}_E$. If $\delta^{(1)} E_k$ is non-zero, it regulates the sign of δE_k, so that stability is assured in this case if for all permissible $\boldsymbol{D}_o$ in (30a)

$$\delta^{(1)} E_k < 0. \tag{31}$$

However, when $\delta^{(1)} E_k$ does vanish, δE_k is dominated by $\delta^{(2)} E_k$, and we require for stability that

$$\delta^{(2)} E_k < 0 \tag{32}$$

for all $\boldsymbol{D}_o$ in (30b).

Now, often, the leading order term $\delta^{(1)} E_k$ is taken to be identically zero. The underlying assumption is the vanishing at equilibrium of the right-hand side of (7a). However, this tacitly assumes that the frame $\mathcal{O}$'s rotation $\boldsymbol{\omega}$ and the average stress field $\bar{\boldsymbol{\sigma}}$ remain unaffected by the velocity perturbation, i.e., $\boldsymbol{\omega}_E$ and $\bar{\boldsymbol{\sigma}}_E$ just before perturbation equal, respectively, $\boldsymbol{\omega}_0$ and $\bar{\boldsymbol{\sigma}}_0$ immediately after. Both these facts may *not* hold. Indeed, as discussed in Section 5.1, the frame $\mathcal{O}$'s rotation rate may have to change instantly to accommodate angular momentum introduced by a general velocity perturbation. Similarly, the stress tensor may jump across $t = 0$. For example, pressure changes instantly in incompressible materials for every perturbation. This is exemplified in the context of homogeneously deforming incompressible ellipsoids by formula (49) in Sharma et al. (2009). Similarly, in *rigid*-plastic materials the stress changes instantaneously when the imposed velocity perturbation is incompatible; see Fig. 1. A simple example is afforded by the frictional slider. Suppose such a slider is at equilibrium while pulled towards the right. The frictional force then acts towards the left. However, if the slider is given a velocity perturbation towards the left, the frictional force *instantly* switches towards the right!

Paper II discusses the above issues in detail. From the discussion there, we find that rotating self-gravitating asteroids are secularly *un*stable at first-order, i.e., we may find a $\boldsymbol{D}_o$ such that $\delta^{(1)} E_k > 0$, if perturbations are allowed to add angular momentum; but see footnote 4 on page 5. For angular momentum-preserving, but incompatible, perturbations

$$\delta^{(1)} E_k = -(\bar{\boldsymbol{\sigma}}_0 - \bar{\boldsymbol{\sigma}}_E) : \boldsymbol{D}_o V, \tag{33}$$

which is guaranteed positive by the *maximum dissipation postulate*; see, e.g., Lubliner (1990, p. 117). Thus, in this case the asteroid is secularly stable at first-order. Note that the maximum dissipation postulate may only be invoked if we assume, as we have, an associative flow rule. For a *non*-associative rigid-plastic material, as Hill (1957) notes, there is strong reason to expect secular instability. This explains an earlier statement in Section 3 about these materials being trivially unstable. Finally, for compatible perturbations that do not add angular momentum, both stress and the coordinate frame's rotation rate are continuous across the perturbation, and, consequently, $\delta^{(1)} E_k$ vanishes. Then δE_k's sign is dictated by $\delta^{(2)} E_k$'s, and, hence, so also is the asteroid's secular stability.

To summarize, we restrict ourselves to a subset of the initial velocity perturbations (28) that do not add angular momentum. Of this subset, a rigid-plastic asteroid, irrespective of the flow rule's choice, is secularly stable at first-order to those perturbations that are incompatible to the equilibrium stress state. Thus, we need only investigate stability to compatible angular-momentum preserving perturbations, and this is decided by $\delta^{(2)}E_k$'s sign, which depends on the underlying flow rule.

We now specialize the above stability test to rubble-pile ellipsoids.

6. Example: Rubble-pile ellipsoids

We model isolated asteroids as self-gravitating ellipsoids rotating about their shortest axis $\hat{e}_3$. Expanding all derivatives in (30b) yields

$$\delta^{(2)}E_k = \left\{ -\dot{\bar{\sigma}}_0 V - \bar{\sigma} \dot{V}_0 + \dot{\boldsymbol{M}}_0^T - (\ddot{\boldsymbol{\Omega}}_0 + \dot{\boldsymbol{\Omega}}_0 \cdot \boldsymbol{\Omega}_E + \boldsymbol{\Omega}_E \cdot \dot{\boldsymbol{\Omega}}_0) \cdot \boldsymbol{I} - (\dot{\boldsymbol{\Omega}}_0 + \boldsymbol{\Omega}_E^2) \cdot \dot{\boldsymbol{I}}_0 \right\}$$
$$: \boldsymbol{D}_o + \left\{ -\bar{\sigma}_0 V + \boldsymbol{M}^T - (\dot{\boldsymbol{\Omega}}_0 + \boldsymbol{\Omega}_E^2) \cdot \boldsymbol{I} \right\} : \dot{\boldsymbol{L}}_0^T,$$

where, because we provide velocity perturbations, objects such as V, $\boldsymbol{I}$ and $\boldsymbol{M}$ retain there equilibrium values at $t = 0^+$. In the above, we replace $\dot{\boldsymbol{L}}$ from (7a), $\dot{\boldsymbol{I}}$ from (7b), $\boldsymbol{M}$ and $\dot{\boldsymbol{M}}$ from, respectively, (21) and its derivative, and $\dot{\rho}$ and $\dot{V}$ from (20). Finally, recalling from the preceding section's end that $\boldsymbol{D}_o$'s and the ellipsoid's principal axes coincide, we obtain

$$\delta^{(2)}E_k = -(\dot{\bar{\sigma}}_0 + \bar{\sigma}_E \mathrm{tr}\boldsymbol{D}_o - 2\bar{\sigma}_E \cdot \boldsymbol{D}_o)$$
$$: \boldsymbol{D}_o V - \left\{ 2\pi\rho G \left(\dot{\boldsymbol{A}}_0 - \boldsymbol{A}\mathrm{tr}\boldsymbol{D}_o \right) + 4\boldsymbol{\Omega}_E \cdot \dot{\boldsymbol{\Omega}}_0 \right\} \cdot \boldsymbol{I} : \boldsymbol{D}_o - \dot{\boldsymbol{\Omega}}_0^2 : \boldsymbol{I}.$$

We also require that the perturbations be compatible. Compatibility depends on the asteroid's chosen rheology and enforces further restrictions on $\boldsymbol{D}_o$; cf. Section 6.3. Computing $\dot{\boldsymbol{A}}$ is complicated and is done in the Appendix A of Paper II. The term involving the stress' time rate of change $\dot{\bar{\sigma}}$ is addressed next.

Section 3 models granular aggregates as rigid-perfectly-plastic materials following an associative flow rule. Post-yield average stress $\bar{\sigma}$ is obtained by volume averaging (17). Differentiating this, we find

$$\dot{\bar{\sigma}}_0 = -\dot{p}_0(1+\epsilon)\boldsymbol{1} + \dot{p}_0\sqrt{k^2 + 3\epsilon^2}\frac{\boldsymbol{D}_o}{|\boldsymbol{D}_o|} + \bar{p}_0$$
$$\times \sqrt{k^2 + 3\epsilon^2}\left\{ \frac{\dot{\boldsymbol{D}}_0}{|\boldsymbol{D}_o|} - \frac{(\dot{\boldsymbol{D}}_0 : \boldsymbol{D}_o)\boldsymbol{D}_o}{|\boldsymbol{D}_o^3|} \right\},$$

so that, after volume-averaging (19) and substituting for $\dot{p}_0$, we obtain

$$\dot{\bar{\sigma}}_0 : \boldsymbol{D}_o = -\kappa\left\{ \sqrt{k^2 + 3\epsilon^2}|\boldsymbol{D}_o| - (1+\epsilon)\mathrm{tr}\boldsymbol{D}_o \right\}\mathrm{tr}\,\boldsymbol{D}_o.$$

Replacing the above in the corresponding term in $\delta^{(2)}E_k$'s expression, we find

$$\delta^{(2)}E_k = \kappa\left\{ \sqrt{k^2 + 3\epsilon^2}|\boldsymbol{D}_o| - (1+\epsilon)\mathrm{tr}\boldsymbol{D}_o \right\}\mathrm{tr}\,\boldsymbol{D}_o V - (\bar{\sigma}_E \mathrm{tr}\,\boldsymbol{D}_o - 2\bar{\sigma}_E \cdot \boldsymbol{D}_o)$$
$$: \boldsymbol{D}_o V - \left\{ 2\pi\rho G (\dot{\boldsymbol{A}}_0 - \boldsymbol{A}\mathrm{tr}\boldsymbol{D}_o) + 4\boldsymbol{\Omega}_E \cdot \dot{\boldsymbol{\Omega}}_0 \right\} \cdot \boldsymbol{I} : \boldsymbol{D}_o - \dot{\boldsymbol{\Omega}}_0^2 : \boldsymbol{I}.$$

We employ this formula to test $\delta^{(2)}E_k$'s sign, and thereby the ellipsoidal granular aggregate's secular stability to all compatible angular momentum-preserving homogeneous perturbations. First, we non-dimensionalize the above expression.

6.1. Non-dimensionalization

We non-dimensionalize $\delta^{(2)}E_k$ by rescaling time by $1/\sqrt{2\pi\rho_0 G}$, stress by $(3/20\pi)\,(2\pi\rho_0 Gm)(4\pi/3V)^{1/3}$, and inertia by $ma_1^2/5$. We obtain

$$\delta^{(2)}E_k = \left[\kappa\left\{ \sqrt{k^2 + 3\epsilon^2}|\boldsymbol{D}_o| - (1+\epsilon)\mathrm{tr}\boldsymbol{D}_o \right\}\mathrm{tr}\boldsymbol{D}_o \right.$$
$$\left. -(\bar{\sigma}_E \mathrm{tr}\,\boldsymbol{D}_o - 2\bar{\sigma}_E \cdot \boldsymbol{D}_o):\boldsymbol{D}_o](\alpha\beta)^{2/3} - \left(\dot{\boldsymbol{A}}_0 - \boldsymbol{A}\mathrm{tr}\boldsymbol{D}_o + 4\boldsymbol{\Omega}_E \cdot \dot{\boldsymbol{\Omega}}_0 \right) \cdot \boldsymbol{Q}:\boldsymbol{D}_o - \dot{\boldsymbol{\Omega}}_0^2:\boldsymbol{Q}, \quad (34)$$

where the derivatives are now with respect to non-dimensional time, $\boldsymbol{Q}$ is a non-dimensional tensor obtained from $\boldsymbol{I}$ that, in the ellipsoid's principal axes coordinate system, has the form

$$[\boldsymbol{Q}] = \begin{bmatrix} 1 & 0 & 0 \\ 0 & \alpha^2 & 0 \\ 0 & 0 & \beta^2 \end{bmatrix}, \quad (35)$$

and $\delta^{(2)}E_k$, κ, $\boldsymbol{D}_o$, $\boldsymbol{\Omega}$ and $\bar{\sigma}$ now represent non-dimensional quantities. In particular, the scaled κ is obtained by dividing a body's plastic modulus by $(3/20\pi)\,(2\pi\rho_0 Gm)(4\pi/3V)^{1/3}$. Thus, κ scales inversely as the square of the object's size; a body twice the size of another of the same material will have one fourth the non-dimensionalized plastic bulk modulus κ.

6.2. Components

To evaluate (34) we need to select an appropriate coordinate system. Because all quantities in $\delta^{(2)}E_k$'s expression refer to the state just after the perturbation, the most convenient choice is the ellipsoid's principal axes coordinate system. In this coordinate system,

$$[\boldsymbol{A}] = \begin{bmatrix} A_1 & 0 & 0 \\ 0 & A_2 & 0 \\ 0 & 0 & A_3 \end{bmatrix}, \quad [\boldsymbol{\Omega}_E] = \begin{bmatrix} 0 & -\omega_E & 0 \\ \omega_E & 0 & 0 \\ 0 & 0 & 0 \end{bmatrix} \quad \text{and} \quad (36)$$

$$[\bar{\sigma}_E] = \begin{bmatrix} \bar{\sigma}_1 & 0 & 0 \\ 0 & \bar{\sigma}_2 & 0 \\ 0 & 0 & \bar{\sigma}_3 \end{bmatrix}$$

with $\bar{\sigma}_i$ to be found in the following section, and for angular momentum-preserving homogeneous perturbations,

$$[\boldsymbol{D}_o] = \begin{bmatrix} D_1 & 0 & 0 \\ 0 & D_2 & 0 \\ 0 & 0 & D_3 \end{bmatrix}. \quad (37)$$

Note that $[\boldsymbol{Q}]$ is already available from (35).

We next obtain the asteroid's equilibrium stress state in this coordinate system, and also identify compatible perturbations.

6.3. Equilibrium and compatible perturbations

The equilibrium stress $\bar{\sigma}_E$'s non-dimensional components in the ellipsoid's principal axes system are found from (22) and adopting Section 6.1's scaling:

$$\bar{\sigma}_1 = (\omega_E^2 - A_1)(\alpha\beta)^{-2/3}, \quad (38a)$$

$$\bar{\sigma}_2 = \alpha^2(\omega_E^2 - A_2)(\alpha\beta)^{-2/3}, \quad \text{and} \quad (38b)$$

$$\bar{\sigma}_3 = -\beta^2 A_3(\alpha\beta)^{-2/3}; \quad (38c)$$

note that shear stresses are zero. The equilibrium pressure $\bar{p}_E$ may now be obtained with the help of (8).

Velocity perturbations are compatible with the stress state only if their associated strain rates are normal to the plastic potential, here taken to coincide with the yield surface. Thus, the strain rates must satisfy the flow rule (14). Eliminating the proportionality constant $\dot{q}$, we find that a homogenous perturbation (28) is compatible when

$$\frac{D_2}{D_1} = \frac{\bar{\sigma}_2 + \bar{p}_E(1+\epsilon)}{\bar{\sigma}_1 + \bar{p}_E(1+\epsilon)} \quad \text{and} \quad \frac{D_3}{D_1} = \frac{\bar{\sigma}_3 + \bar{p}_E(1+\epsilon)}{\bar{\sigma}_1 + \bar{p}_E(1+\epsilon)}; \quad (39)$$

note that the shear strain rates are zero. Thus, a compatible perturbation automatically preserves the asteroid's angular momentum at equilibrium.

We now return to the stability analysis of rubble-pile asteroids.

6.4. Local stability

The stability of rotating inviscid fluid ellipsoids corresponding to $\phi_F = 0_o$ is considered in detail in Paper II. There it is found that the stability test developed above predicts that Maclaurin spheroids are secularly stable for axes ratio $\beta \geqslant \beta_J = 0.5827$; this being the *Jacobi point* from where the Jacobi sequence of ellipsoids bifurcate from the Maclaurin sequence. All Jacobi ellipsoids were found to be secularly stable. These results are consistent with those of Jeans (1961) and Lyttleton (1953) who invoked the Lagrange–Dirichlet theorem, and of Chandrasekhar (1969) who employed spectral analysis. Chandrasekhar (1969) further showed that Maclaurin spheroids are *ordinarily*[5] stable for $\beta_R \leqslant \beta \leqslant \beta_J$, where $\beta_R = 0.3033$ is the *Riemann point* from where the sequence of Riemann ellipsoids emerge from the Maclaurin equilibrium curve; spheroids with $\beta < \beta_R$ were ordinarily unstable. Between $\beta_R \leqslant \beta \leqslant \beta_J$ the Maclaurin spheroids are stabilized by gyroscopic forces. Recall that these forces do not input any power and are hence ignored by the energy criterion, leading us to predict secular *in*stability for $\beta \leqslant \beta_J$. It is interesting to note that Rosenkilde (1967) showed that these gyroscopically stabilized Maclaurin spheroids are, in fact, rendered unstable by viscosity's presence. Finally, Paper II also draws attention to an apparent contradiction, which is subsequently resolved, between the predictions of Riemann about the stability of Maclaurin spheroids and those of Jeans, Lyttleton and Chandrasekhar. After this brief summary of the stability of fluid ellipsoids as determined by our stability criterion, we move on to granular ellipsoids.

We saw in Section 4 that rubble-pile ellipsoids with a given internal friction angle ϕ_F may persist in equilibrium in a three-dimensional volume bound by an upper and a lower critical surface associated with ϕ_F's choice. This is in marked contrast to inviscid fluids where equilibria were identified by three-dimensional curves in $\alpha - \beta - \omega_E$ space.[6] Thus, for rubble-pile ellipsoids rotating at ω_E and with friction angle ϕ_F, we have to test the stability of ellipsoids that lie not only on the associated critical surfaces, but also within.

By an application of the maximum dissipation postulate, it may be shown that all ellipsoids that lie within the equilibrium zone corresponding to their internal friction, and not on the associated critical surface, are necessarily *stable* at *first*-order to compatible perturbations. Indeed, consider an ellipsoid at equilibrium but not on the critical surface. Then the average equilibrium stress $\bar{\boldsymbol{\sigma}}_A$ lies within the yield surface of Fig. 1. When perturbed by $\boldsymbol{D}_B$ that satisfies (39) for some compatible stress $\bar{\boldsymbol{\sigma}}_B$ that lies on the yield surface, the ellipsoid's stress state switches immediately to $\bar{\boldsymbol{\sigma}}_B$ from $\bar{\boldsymbol{\sigma}}_A$. This leads to $\delta^{(1)} E_k = -(\bar{\boldsymbol{\sigma}}_B - \bar{\boldsymbol{\sigma}}_A) : \boldsymbol{D}_B$ that is guaranteed positive by the maximum dissipation postulate. It remains, therefore, to consider the stability to compatible perturbations of only those granular ellipsoids that at equilibrium lie on the critical surface associated with their internal friction. We identify these as *critically equilibrated ellipsoids*. We will explore their stability by considering two-dimensional sections of the equilibrium landscape corresponding to oblate, prolate and average-triaxial ellipsoids.

Fig. 3 displays stability results for oblate ellipsoids for various choices of the scaled plastic bulk modulus κ. For each κ, there is associated a shaded region within which all critically equilibrated
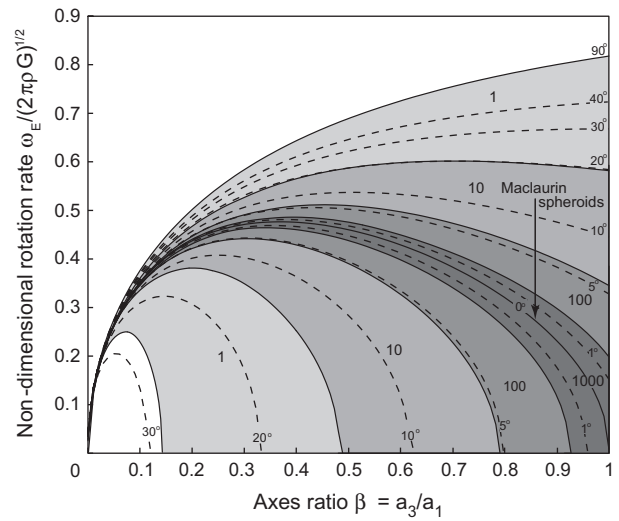

Fig. 3. Stability regions in shape (β)–spin (ω_E) space for oblate ellipsoids with $\alpha = 1$. Several different non-dimensional plastic bulk moduli κ are explored, and the corresponding stability regions are shaded. Also shown by dotted lines are the equilibrium zones corresponding to various choices of internal friction angle ϕ_F; these equilibrium curves follow Fig. 5 of Paper I. The stability region corresponding to $\kappa = 1$ is limited by the $\phi_F = 90°$ disruption curve.

ellipsoids are secularly stable. Equivalently, ellipsoids lying on their corresponding critical equilibrium curve outside the shaded stability region associated with their plastic bulk modulus will be secularly unstable. Figs. 4 and 5 display stability regions for critically equilibrated prolate and average triaxial ellipsoids, respectively. It is interesting to note in Fig. 5 that the stability region appears to shrink to the Jacobi ellipsoid as $\kappa \to \infty$. This suggests that a stable critically equilibrated *incompressible* granular ellipsoid must have zero internal friction, i.e., is an *inviscid* incompressible fluid.

In each of the three figures above, we see that as the plastic bulk modulus is *lowered*, the stability regions *expand*, with the lower-κ stability region containing the higher-κ zone as a subset. To understand this, we recall from (10) that at a given pressure, the equilibrium zone grew with increasing internal friction, allowing the body
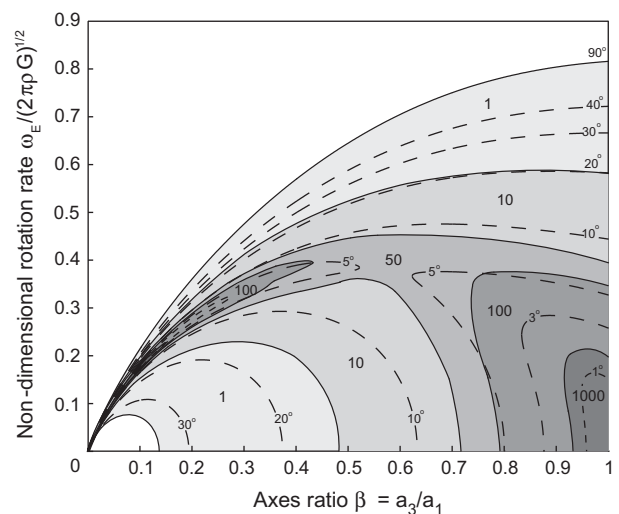

Fig. 4. Stability regions for several non-dimensional plastic bulk moduli κ in shape (β)–spin (ω_E) space for prolate ellipsoids with $\alpha = \beta$. The dotted lines indicate equilibrium zones for various choices of internal friction angle ϕ_F; these follow Fig. 6 of Paper I. See also Fig. 3's caption.

---

[5] Systems found (un)stable by the spectral method are ordinarily (un)stable.
[6] This holds also for Riemann ellipsoids that have internal vortical motion but constant shape; see Chandrasekhar (1969, p. 129).
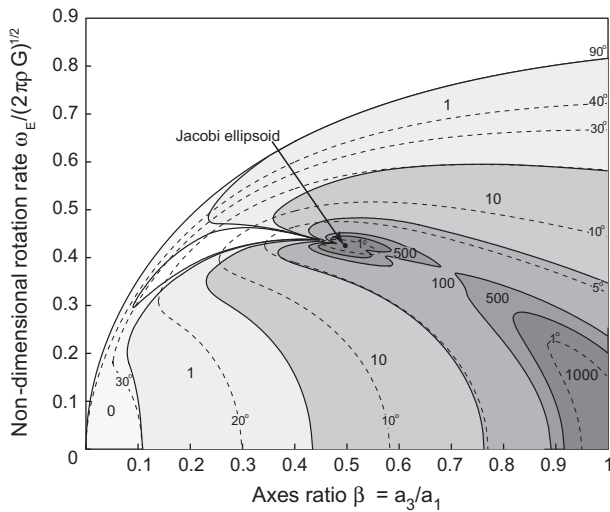
Fig. 5. Stability regions for several non-dimensional plastic bulk moduli κ in shape (β)–spin (ω_E) space for average-triaxial ellipsoids with $\alpha = (1 + \beta)/2$. The dotted lines indicate equilibrium zones for various choices of internal friction angle ϕ_F; these follow Fig. 7 of Paper I. See also Fig. 3's caption.

to achieve shapes and spins that coincided with ever greater principal shear stresses; cf. (12). Thus, if the internal friction of a critically equilibrated ellipsoid was lowered, it would yield and the ellipsoid would adapt its shape and spin so as to move within the equilibrium zone corresponding to the lowered value of internal friction. Because pressure plays a role analogous to internal friction, exactly the same response will be observed if the pressure within a critically equilibrated ellipsoid was to suddenly reduce; the ellipsoid will attempt to move within an equilibrium region closer to that of a fluid. We expect that the ellipsoid's excursions from its equilibrium will be slow and modest for small pressure drops. On the other hand, if the pressure is significantly lowered, the ellipsoid will move faster and closer to a state with low shear stress, i.e., nearer to a fluid's equilibrium curve. Now, we saw from (18) that the material post-yield expands and this, from our constitutive postulate (19) led to a subsequent drop in the pressure from its equilibrium value. The pressure drop's extent is proportional to the plastic bulk modulus κ. Therefore, for large κ, ellipsoid's far away from the equilibrium curve of fluid ellipsoids will be found unstable. Equivalently, ellipsoids with smaller plastic bulk moduli will have larger stability regions.

6.5. Stability to finite perturbations

We have so far considered a system stable if the leading estimate of the relative kinetic energy δE_k's change is negative. This is satisfactory when perturbations are infinitesimally small. However, in the presence of finite perturbations it may happen that δE_k increases/decreases following an initial decline/rise. This will indicate higher-order instability/stability. We explore it in the context of ellipsoids whose stress state at equilibrium lies within the yield surface, and so are predicted to be stable at first-order. Such an analysis is interesting considering the improbability of finding critically equilibrated asteroids.

Consider a rotating self-gravitating rubble-pile ellipsoid whose stress state at equilibrium lies within, and not on, the yield surface, i.e., the ellipsoid's location in shape–spin space is inside its associated equilibrium zone, and not on its boundary. We saw that the maximum dissipation postulate assures first-order local stability for this ellipsoid. Thus, for small enough δt, $\delta E_k^{(1)}$ is negative and it regulates δE_k's sign as well. However, if we follow δE_k's evolution, it may happen that beyond a time $\delta t^* \sim 2|\delta^{(1)} E_k / \delta^{(2)} E_k|$, $\delta^{(2)} E_k$'s

contribution $\delta^{(2)} E_k \delta t^2 / 2$ overcomes $\delta^{(1)} E_k$'s. In this case, if $\delta^{(2)} E_k > 0$, δE_k will become positive for times greater than δt^*, and the system, though locally confined over infinitesimal displacements, may begin to depart from its equilibrium location after time δt^*; such a situation will be considered unstable. Obviously, greater $\delta^{(2)} E_k$ is in comparison to $\delta^{(1)} E_k$, smaller is δt^*, i.e., the earlier this instability will occur. Thus, ellipsoids that, while not critically equilibrated, but lying in regions wherein $\delta^{(2)} E_k$ is positive may be *unstable* to perturbations large enough to ensure that the system does not cease moving before time δt^*.

The expression for $\delta^{(2)} E_k$ for ellipsoids whose average stress state $\bar{\boldsymbol{\sigma}}_E$ at equilibrium does not lie on the yield surface may be obtained in a manner similar to how (34) was derived. We find that

$$
\begin{aligned}
\delta^{(2)} E_k = &[\kappa\{\sqrt{k^2 + 3\epsilon^2}|\boldsymbol{D}_o| - (1 + \epsilon)\mathrm{tr}\boldsymbol{D}_o\}\mathrm{tr}\boldsymbol{D}_o - (\bar{\boldsymbol{\sigma}}_0 \mathrm{tr}\boldsymbol{D}_o \\
&- 2\bar{\boldsymbol{\sigma}}_E \cdot \boldsymbol{D}_o) \\
&: \boldsymbol{D}_o](\alpha\beta)^{2/3} - (\dot{\boldsymbol{A}}_0 - \boldsymbol{A}\mathrm{tr}\,\boldsymbol{D}_o + 4\boldsymbol{\Omega}_E \cdot \dot{\boldsymbol{\Omega}}_0) \cdot \boldsymbol{Q} : \boldsymbol{D}_o - \dot{\boldsymbol{\Omega}}_0^2 \\
&: \boldsymbol{Q} + \Delta\bar{\boldsymbol{\sigma}} : \left(\boldsymbol{D}_o^2 + \boldsymbol{Q}^{-1} \cdot \Delta\bar{\boldsymbol{\sigma}}\right)(\alpha\beta)^{2/3},
\end{aligned} \tag{40}
$$

where the change in the equilibrium stress to its post-perturbation value $\bar{\boldsymbol{\sigma}}_0$,

$$
\Delta\bar{\boldsymbol{\sigma}} = \bar{\boldsymbol{\sigma}}_0 - \bar{\boldsymbol{\sigma}}_E = \bar{\boldsymbol{s}}_E + \frac{k\bar{p}_E - |\bar{\boldsymbol{s}}_E|}{|\bar{\boldsymbol{s}}_E|}\bar{\boldsymbol{s}}_E,
$$

is obtained by scaling the equilibrium deviatoric stress $\bar{\boldsymbol{s}}_E$ so that $\bar{\boldsymbol{s}}_0$ lies on the yield surface; thus, there is no change in the pressure. This choice guarantees the smallest possible value for $\delta^{(1)} E_k$. Note that $\bar{\boldsymbol{s}}_E$ is available from (38) and (9) once the rotation rate ω_E and the ellipsoid's shape are chosen. Note that in the above development, the states 'E' and '0' correspond to locations A and B of Fig. 1, respectively.

Figs. 6 and 7 display regions in shape–spin space where $\delta^{(2)} E_k$ given by (40) is negative for, respectively, prolate and average-triaxial ellipsoids with an internal friction angle ϕ_F of $30°$. The regions are parameterized by the non-dimensional plastic bulk modulus κ. We observe that, in general, as the plastic bulk modulus κ increases from 0 to about 10, the region where $\delta^{(2)} E_k$ is negative shrinks. For some κ this zone vanishes. As κ continues to increase, this region reappears and begins to grow. For κ beyond 1000, these regions tend not to change. This is because for large κ, the first term in $\delta^{(2)} E_k$'s expression that is regulated by κ controls
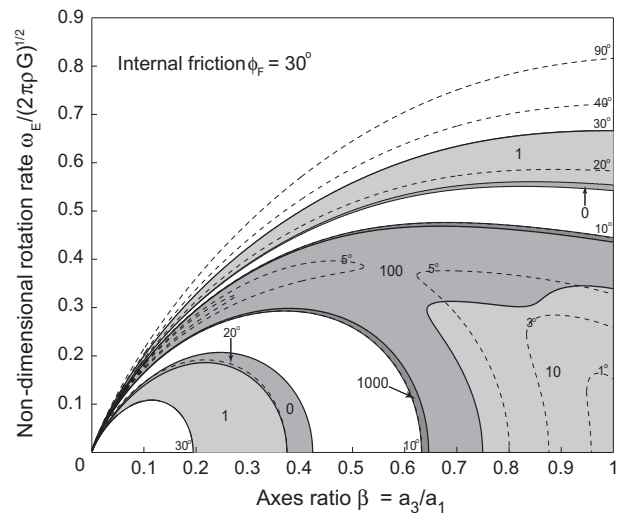

Fig. 6. Regions in shape (β)–spin (ω_E) space where $\delta^{(2)} E_k < 0$ for prolate ellipsoids with $\alpha = \beta$ and internal friction angle $\phi_F = 30°$. The shaded regions correspond to different non-dimensional plastic bulk moduli κ. See also Fig. 4's caption.
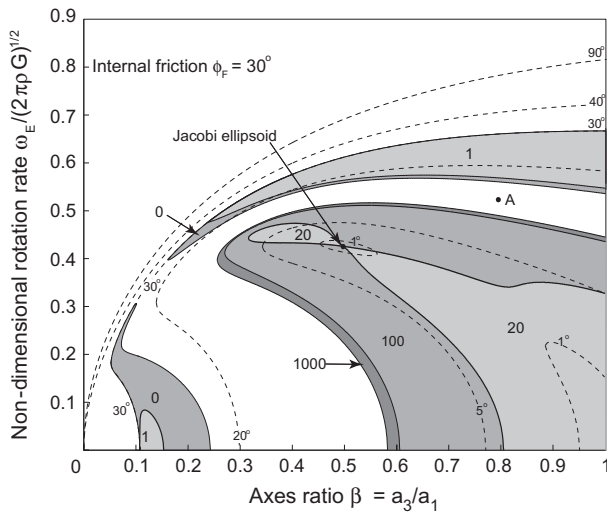
Fig. 7. Regions in shape (β)–spin (ω_E) space where $\delta^{(2)}E_k < 0$ for average-triaxial ellipsoids with $\alpha = (1 + \beta)/2$ and internal friction angle $\phi_F = 30°$. The shaded regions correspond to different non-dimensional plastic bulk moduli κ. The point marked '*A*' is an example asteroid discussed in the text. See also Fig. 5's caption.
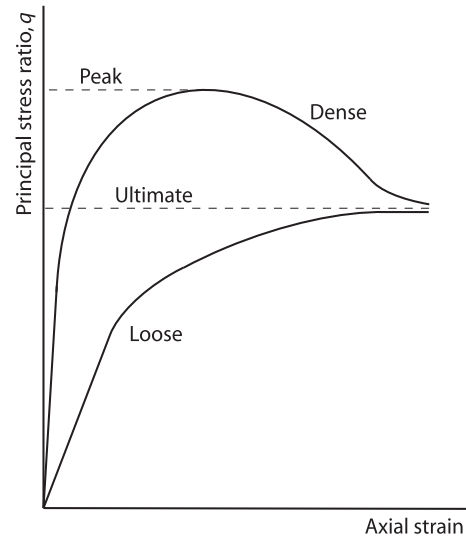

Fig. 8. Typical variation with axial compression of the ratio q of the axial and lateral stresses during triaxial tests of initially dense and loose soils.

$\delta^{(2)}E_k$'s sign. Note that because we have taken the ellipsoids to have $\phi_F = 30°$, the stability regions do not extend beyond the equilibrium zone corresponding to a friction angle of 30°.

As an illustration, consider asteroid *A* with internal friction angle $\phi_F = 30°$ located as shown in Fig. 7. Assume that the asteroid has a plastic bulk modulus of 1 MPa and density 2000 kg m^{-3}. If the asteroid's largest semi-major axis were 2 km, its non-dimensional plastic bulk modulus κ would be slightly more than 900. Because *A* is within the equilibrium region corresponding to $\phi_F = 30°$, the results of the previous section guarantee its local secular stability at first-order to infinitesimal perturbations. However, its location in Fig. 7 confirms that $\delta^{(2)}E_k > 0$, so that there is a possibility that *A* may deform appreciably following a finite perturbation. On the other hand, were *A*'s rotation rate lower, so that it lay within the shaded region corresponding to κ of 1000, $\delta^{(2)}E_k$ would be negative. In that case, the asteroid *A* would be stable to finite, and not just infinitesimal, disturbances.

Similar arguments may be made to motivate the impact of still higher-order corrections to δE_k.

7. Application: Near-Earth asteroids

7.1. Material parameters

Granular materials like soils display extremely complex stress response, and constitutive models such as the popular cam-clay model rely on very many parameters to capture this complexity; see, e.g., Bolton (2003, p. 210). However, given that very little is known about the physical nature of asteroids, utilizing a material model with many parameters appears unwarranted. Thus, here we model the material response of dry granular aggregates as a rigid-perfectly plastic material with only two constitutive parameters, viz., the internal friction angle ϕ_F that defines the yield surface, and the plastic bulk modulus κ that describes the flow post-yield. Both these parameters depend on the manner in which the aggregate is packed and the properties of its constituent grains. For dry materials, the aggregate's packing may be described in terms of its *void ratio*[7] and the average pressure *confining* the aggregate together.

---

[7] Ratio of the free volume in an aggregate to the volume occupied by grains.

A popular and versatile method of probing soils is the *triaxial test*; see, e.g., Bolton (2003, p. 189), for a detailed description. The setup involves first confining a sack containing sand at some void ratio at an initial pressure by immersing it in a fluid. The sack is then sheared by compressing it incrementally along its axis; the axial and lateral directions are then the principal stress/strain directions. The internal friction angle ϕ_F is found by measuring the ratio q of the axial to the lateral principal stress at yield, and invoking the formula $\phi_F = \sin^{-1}[(q - 1)/(q + 1)]$. A typical response of the principal stress ratio q's variation with axial compression during a single triaxial test is shown in Fig. 8. We observe from Fig. 8 that q goes through a maximum before settling into a lower limiting value. The maximum of q corresponds to the soil's *peak* strength, while its limiting value is the soil's *ultimate* strength. The soil is said to have yielded when its peak strength is reached. It then subsequently *softens* to a final *critical* state. A soil's critical state is characterized by an ultimate friction angle and a void ratio that depends only on the confining pressure and not the soil's initial density; see, e.g., Bolton (2003, Section 4.4, p. 69). Initially loose soils often do not display a peak strength, and asymptotically reach their critical state; see Fig. 8. The bulk modulus κ is found by the *hydrostatic compression test* that involves imposing additional hydrostatic loading on the same initial triaxial setup. It is found that a soil's bulk modulus, and its peak and ultimate friction angles depend crucially on the confining pressure, while only the first two depend on the initial void ratio. These values can vary appreciably from one soil to another.

Here, we employ the ultimate friction angle as the internal friction angle ϕ_F that characterizes yield in our rigid-perfectly plastic material model. There are several reasons for doing so. First, as mentioned above, a soil's peak strength depends on in its initial density, but not so its ultimate strength. Dense soils display a peak strength, while loose soils do not. In contrast, every soil realizes its ultimate (critical) state. Furthermore, as the experiments cited below report, while the peak behavior varies greatly depending on the soil type, the ultimate strength changes little and remains within 30–40°. Thus, given that we do not know much about asteroidal interiors or origins, it appears prudent to calibrate our theory against a soil's critical state that differs less across soils, initial states and confining pressures. Second, the decrease in the frictional strength post-peak may be modeled by including softening within our material model. An application of the maximum

dissipation postulate will then show that a softening rigid-plastic material is trivially locally unstable at first order; see, e.g., Chen and Han (1988, Section 3.6.3, p. 168). Thus, we are less likely to find asteroids with shapes and spins at equilibrium that require the asteroid to mobilize its peak frictional strength. Finally, though we do not investigate a granular asteroid's long-term dynamics, it is clear that it will be dictated by the asteroid's ultimate friction angle.

Typically, experiments are done at confining pressures of one or more MPa and sand is found to have an ultimate friction angle ϕ_F between 30–40° and plastic bulk modulus κ of 1 MPa. The ultimate friction angle for dense sands, though higher than ϕ_F is also within the same range of 30–40°. On the other hand, not much experimental data is available on sand confined at lower pressures. Ponce and Bell (1971) and Fukushima and Tatsuoka (1984) report triaxial tests conducted at confining pressures between, respectively, 1.4 and 241 kPa, and 2 and 400 kPa. These two tests utilized possibly the lowest confining pressures in terrestrial triaxial tests done till date. Recently, Sture et al. (1998) performed tests in space shuttle flights under low-gravity conditions at confining pressures of 0.05, 0.52 and 1.30 kPa.

Ponce and Bell (1971) reported that as the confining pressure reduced from about 35 kPa to 1.4 kPa the ultimate internal friction angle ϕ_F increased sharply from about 30° to 44°. The corresponding value of peak friction for 'very dense' sands changed from 38.5° to 51.5°. This was attributed to reduced grain crushing during shearing at low pressures. For 'very loose' sands the peak and ultimate frictional strengths coincided, and was explained on the basis of lowered resistance to particle motion by neighboring particles. For the quartz sand that Ponce and Bell (1971) employed, the *relative density*[8] for very loose sands was 5%, and was 94% for very dense ones; the corresponding void ratios are 0.71 and 0.48, respectively. On the other hand, the careful triaxial tests of Fukushima and Tatsuoka (1984) that were conducted at low confining pressures between 2 kPa and 10 kPa, but on a different (Toyura) sand, concluded that the ultimate friction angle ϕ_F changed slightly from 33.5° to 35°. The peak strength of Toyura sand did increase as the initial void ratio was lowered, but remained invariant to changes in the confining pressures at a fixed void ratio. In fact, the peak friction angle in dense Toyura sand was found almost constant at about 43.5°. This latter conclusion was at variance with that of Ponce and Bell (1971), and emphasized the difference in the material response of different soils, especially at low confining pressures. Finally, working with Ottawa quartz sand, Sture et al. (1998) confirmed the trends of the terrestrial experiments of Ponce and Bell (1971). Sture et al. (1998) found that in sand with relative density 85% the peak friction angle increased from 53.3° to 63.4° as the confining pressure fell from 1.30 kPa to 0.05 kPa. At the same time, in 20% less dense soils, the peak friction grew from 47.6° to 70° over the same decrease of confining pressure. The ultimate friction angle ϕ_F's range too increased, albeit slightly, from 32–34° in terrestrial conditions to 35–37° in a micro-gravity environment.

In each of the three works cited above, as the hydrostatic compression test was not conducted, values of bulk modulus are not accessible from the reported data. Hydrostatic compression tests have been carried out at a confining pressure of 20 kPa and 25 kPa by, respectively, Lancelot et al. (2006) and Lade et al. (2009); there appear to be no experiments at lower confining pressures. Lancelot et al. (2006) report a plastic bulk modulus κ of 100 kPa for loose Hotsun RF sand at a void ratio of 0.897 that they employed. In contrast, Lade et al. (2009) observed a much higher κ of 100 MPa for loose Ottawa sand at a void ratio of 0.83, that increased to 200 MPa as the void ratio decreased to 0.62.

We saw above that soil properties show large variation with not only the void ratio and the confining pressure, but also depend crucially on the type of sand employed for experiments. Now, we require values of ϕ_F and κ at void fractions and confining pressures that we expect in rubble-pile asteroids. Assuming an average density of 2 g cm^{-3} for a rubble-pile asteroid, and further assuming chondritic constituent grains with density about 3.2 g cm^{-3} yields a void ratio of 0.6. A terrestrial soil at this void ratio would be labeled 'dense'. The corresponding volume fraction[9] is 0.625, close to the volume fraction 0.64 of randomly closed packed aggregate of same-sized spheres; see Jaeger and Nagel (1992). Similarly, rubble-piles are held together by their own gravity, and thus exist at extremely low confining pressures of the order of tens of Pascals. Indeed, employing (38) and (8) for 25143 Itokawa we compute the average pressure to be as low as 4.3 Pa! This is three orders of magnitude lower than the confining pressure employed in the terrestrial triaxial tests reported above, and four orders lower than the pressure utilized in the hydrostatic compression tests experiments quoted above. The average pressure scales as the square of the size, but even then, the largest near-Earth asteroid Eros has an average internal pressure of a mere 17.7 kPa, still lower than the experiments of Lancelot et al. (2006). This suggests that excepting Sture et al. (1998), most experimental soil data currently available cannot be employed to investigate rubble-pile asteroids and other small Solar System objects; more experiments on dense soils confined at pressures less than 100 Pa are needed.

In passing, we note that it was hoped that experiments on dust aggregates by Blum and Schräpler (2004), done with a view to understand planet formation and comets, would have given some hint at properties of lightly confined aggregates. However, these aggregates are typically very fluffy with volume fractions of about 0.15 increasing to maximum of about 0.34, which is much lower than the volume fraction of 0.625 estimated above for rubble-pile asteroids.

Past work on rubble-pile asteroids, e.g., by Holsapple (2004) and Sharma et al. (2009), has typically assumed ϕ_F about 30°, and a κ of 1 MPa corresponding to a non-dimensional value of about 10000 for a body like Itokawa, but about 100 for a larger asteroid like Eros. However, the discussion above suggests that these numbers may not be sacrosanct. We will, therefore, not ignore the possibility of lightly confined rubble-pile asteroids having greater (ultimate) internal friction angles ϕ_F of 40°/50°. It will also be interesting to consider the possibility of a lower ϕ_F of 20°. This is because dissimilar soils can respond very differently, for example, natural sandy gravel has an ultimate friction angle of about 25°. Furthermore, it is known that previously worked soil may have much lower *residual* frictional strengths of 10–15°; see Bolton (2003, Section 8.7.3, p. 55). Whether such reduction is still observed at low confining pressures still needs to be tested. Finally, as particle rearrangements will require no effort in the absence of a confining pressure there will be no internal frictional resistance, and we therefore expect that there will a regime of low-confining pressures when friction in a soil will be much reduced. Whether this regime exists and is relevant at internal pressures observed in asteroids needs experimental verification. Similarly, plastic bulk moduli of a few kilo-Pascals, corresponding to scaled κ of about 10 for asteroids of size about a kilometer and density 2000 kg m^{-3}, will be worth exploring. Physically, this reflects our expectation that contacts between the constituent grains in these asteroids will be lightly loaded resulting in a lowered plastic bulk modulus.

Before concluding this section, we mention that recent work by Scheeres et al. (2010) suggests that in granular bodies with

---

[8] Ratio of the deviation of the void ratio from its maximum achievable value to the total possible change in the void ratio at a given confining pressure.

[9] Ratio of volume occupied by grains to total volume.

meter-sized or smaller constituent grains, cohesion arising from van der Waals interaction may play a role commensurate with internal gravity. Scheeres et al. (2010) propose that because of these cohesive interactions, the behavior of rubble piles in space may be analogous to powders in terrestrial conditions; this makes the case for performing experiments similar to those of Blum and Schräpler (2004), albeit with denser powders. Cohesive bodies are able to accommodate tensile stresses to some extent, and Holsapple (2007) finds that even a small amount of cohesion may allow small fast rotators to survive as rubble piles. There exist straightforward extensions of the rigid-plastic material model utilized here that may be employed to include cohesive effects; see, e.g., Chen and Han (1988, Section 2.3.4, p. 94). However, we do not pursue this here.

7.2. Near-Earth asteroid data

The rotation rates, density and sizes of several known near-Earth asteroids (NEAs) are listed in Tables 1 and 2 along with, respectively, the axes ratios of their best-fit prolate and average-triaxial ellipsoidal shapes. Both radar and optical observational data were employed. Data for 1980 Tezcatlipoca, 3199 Nefertiti, 3908 Nyx, and 5587 1990 SB were taken from Kaasalainen et al. (2004) who inverted light curves to obtain ellipsoidal shapes that best duplicated their observations. The light curve analysis of Pravec et al. (1998) provided information for the shapes of 1943 Anteros, 3122 Florence, 3752 Camillo, 7025 1993 QA and 11066 Sigurd. Finally, the radar observations and subsequent shape modeling incorporating both radar and, often, optical data, of Magri et al. (2007, 2011), Hudson and Ostro (1994, 1995, 1999), Benner et al. (1997, 1999), Hudson et al. (2000), Busch et al. (2006, 2008, 2011), Vilas et al. (1985), Shepard et al. (2008), and Brozovic et al. (2010a,b, 2011) provided for, respectively, 1580 Betulia, 8567 1996 HW1, 4769 Castalia, 4179 Toutatis, 1620 Geographos, 3103 Eger, 2063 Bacchus, 6489 Golevka, 10115 1992 30 SK, 33342 1998 WT24, 2008 EV5, 3288 Seleucus, 2100 Ra-Shalom, 4660 Nereus, 4486 Mithra, 136617 1994 CCα. Data for 433 Eros and 21543 Itokawa that were visited by probes are taken from, respectively, Veverka et al. (2000), and Fujiwara et al. (2006). In some cases the best-fit ellipsoids were not exactly prolate or average-triaxial, but in keeping with the errors inherent in observations, we ignored the mismatch if it was within 10%. For most asteroids densities are not known and we employ densities as-

Table 1
Prolate asteroids. For each asteroid, its maximum estimated extent d (if known), axes ratio β, density ρ, rotation period P and the corresponding non-dimensional rotation rate ω are given. The axes ratio $\alpha \approx \beta$.

Asteroid	β	ρ (g cm^{-3})	P (h)	ω	d (km)
8567 1996 HW1	0.39	2	8.76	0.22	3.8
1620 Geographos	0.4	2	5.22	0.36	5
2063 Bacchus	0.45	3.6	15.00	0.09	1.11
4769 Castalia	0.44	2.1	4.00	0.47	1.8
3103 Eger	0.65	2	5.70	0.33	2.3
433 Eros	0.33	2.67	5.27	0.31	34.4
4129 Toutatis	0.42	2.1	176.00	0.01	4.6
6489 Golevka	0.71	2.7	6.03	0.27	0.35
4486 Mithra	0.61	2	67.50	0.03	2.35
10115 1992 SK	0.65	2.3	7.32	0.24	1.39
21543 Itokawa	0.44	1.9	12.13	0.16	0.52
3288 Seleucus	0.41	2	75	0.03	3.4
1943 Anteros	0.91	2	2.87	0.66	2.3
3122 Florence	0.83	2	2.36	0.81	4.9
3752 Camillo	0.50	2	37.85	0.05	–
7025 1993 QA	0.77	2	4.21	0.45	–
11066 Sigurd	0.40	2	8.5	0.22	2.5
3908 Nyx	0.83	2	4.43	0.43	1.5
5587 1990 SB	0.42	2	5.05	0.38	3.57

Table 2
Average-triaxial asteroids. For each asteroid, its maximum estimated extent d (if known), axes ratio β, density ρ, rotation period P and the corresponding non-dimensional rotation rate ω are given. The axes ratio $\alpha \approx (1 + \beta)/2$.

Asteroid	β	ρ (g cm^{-3})	P (h)	ω	d (km)
2100 Ra-Shalom	0.66	2.4	19.79	0.09	2.96
1580 Betulia	0.64	2	6.14	0.31	6.59
33342 1998 WT24	0.85	3	3.70	0.42	0.47
2008 EV5	0.93	3	3.73	0.42	0.42
136617 1994 CCα	0.93	2	2.39	0.80	0.69
4660 Nereus	0.47	2	15.16	0.13	0.33
1980 Tezcatlipoca	0.51	2	7.25	0.26	4.3
3199 Nefertiti	0.83	2	3.02	0.63	2.2
4957 Brucemurray	0.83	2	2.89	0.66	–

sumed in earlier work. Exceptions to this include Eros and Itokawa, and asteroids such as Castalia and Toutatis where radar observations coupled with detailed shape models have constrained the density to some extent. Finally, the sizes of Seleucus, Anteros, Florence, Tezcatlipoca and Nefertiti were obtained from Chapman et al. (1994), while Delbo et al. (2003) provided for 1990 SB and Nereus.

We have accepted the shapes and spins coming from the cited sources for lack of better options, but we recognize that they may contain errors. In this light we emphasize that, in the following sections, the aim is primarily to indicate how equilibrium and stability results obtained here may be employed to probe internal structures of asteroids given their shape and spin states. Finally, we note that the importance of accurate size estimates cannot be overemphasized. For example, in his study of the stability of granular asteroids, Holsapple (2004) assumes an average asteroid size of 10 km to rescale elasto-plastic moduli. This is several times the size of known near-Earth asteroids with the exception of Eros; see Tables 1 and 2. As we saw in Section 6.1, moduli are scaled by the inverse square of the object's size, and, because stability depends crucially on plastic modulus, inappropriate rescaling may lead to misleading results.

7.3. Local stability

We consider the stability of rubble asteroids to infinitesimal perturbations. In these cases, we utilize the local stability plots of Section 6.4 that retain the influence of the first-order term $\delta^{(1)} E_k$. Figs. 9 and 10 repeat these stability maps while locating on them, respectively, the asteroids listed in Tables 1 and 2. From Figs. 9 and 10, we may immediately claim that 3122 Florence and 136617 1994 CCα that lie outside or very near the disruption curve corresponding to $\phi_F = 90°$ are not rubble-piles, or if they are, then they have some amount of cohesion that allows them to support tensile stresses. The former conclusion is not very surprising for the 0.8 km diameter 1994 CCα that is the largest member of a triplet system, remnants, perhaps, of an earlier disruption. However, Florence is estimated to be 4.9 km in diameter. This, and its identification as a S-type asteroid, suggests the possibility of it being a granular aggregate, in which case its location in Fig. 9 indicates the presence of cohesion. Asteroids other than the three noted above lie within the equilibrium curve corresponding to an internal friction angle ϕ_F of 30°. In fact, barring 1943 Anteros, 4957 Brucemurray and 3199 Nefertiti, the remaining lie within the $\phi_F = 20°$ equilibrium curve. If, as discussed in Section 7.1, we agree that ϕ_F for aggregates tends to increase from 30° as the confining pressure decreases, then this supports the hypothesis that these objects are rubble piles. On the other hand, if we believe that at extremely low confining pressures ϕ_F may actually fall below 30° due to relative ease in particle rearrangements, then it makes the existence of Anteros, Brucemurray and Nefertiti as cohesionless rubble-piles suspect.
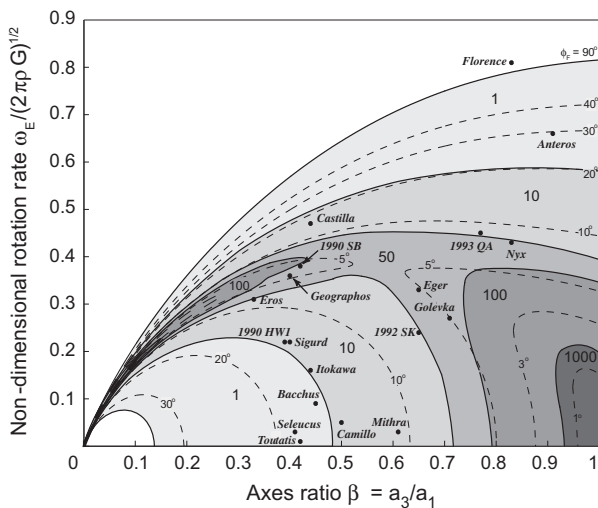
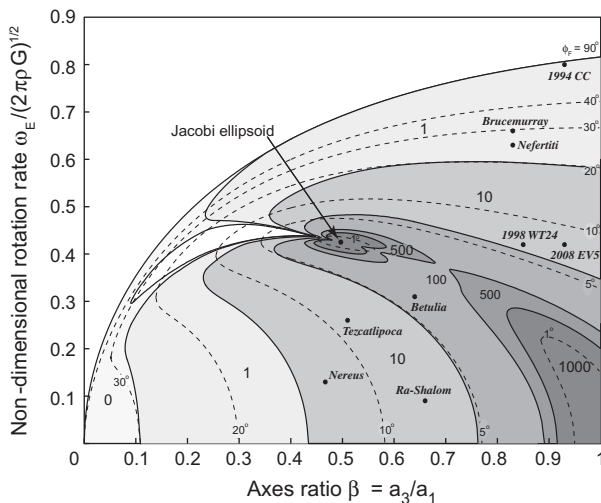**Fig. 9.** Location of prolate NEAs on the stability map of Fig. 4. See also Fig. 4's caption.

Fig. 10. Location of average-triaxial NEAs on the stability map of Fig. 5. See also Fig. 5's caption.

Conclusions about the physical characteristics of asteroids, based on their local structural stability as rubble-piles, is only possible if the asteroid lies on its associated critical equilibrium curve, i.e., the asteroid is critically equilibrated. As we saw in Section 6.4, granular ellipsoidal asteroids whose stress state at equilibrium lies within the yield surface are automatically locally stable at first-order due to the maximum dissipation postulate. Thus, for example, if we assume that Itokawa is a granular aggregate with friction angle $\phi_F \geqslant 30°$, then Fig. 9 shows that it that lies comfortably in the associated equilibrium region's interior. Our stability analysis will find it stable, and nothing may be concluded about its bulk modulus κ, or its existence as a granular aggregate.

Asteroids 1943 Anteros and 4957 Brucemurray allow for more interesting analysis. Figs. 9 and 10 show, respectively, that these asteroids lie very nearly on the equilibrium curve corresponding to an internal friction angle ϕ_F of 30°. If we assume that aggregates confined at extremely low pressures too have ϕ_F around 30°, then both Anteros and Brucemurray are almost critically equilibrated. In that case, to have survived gentle perturbations, perhaps in the form of distant flybys, through the course of their existence these

two asteroids cannot have a scaled κ greater than 10. For the 2.3 km diameter Anteros this corresponds to a maximum plastic bulk modulus of about 4 kPa. This may be an acceptable estimate for Anteros that is confined by an average internal pressure of only 0.14 kPa. A similar estimate may be reached for the bulk modulus of 3199 Nefertiti that in Fig. 9 is shown to lie between the $\phi_F = 30°$ and $\phi_F = 20°$ equilibrium curves, provided we make the not implausible assumption that an extremely low-pressure confined Nefertiti's internal friction is somewhat less than 30°.

In the case of Brucemurray, whose size is not known, we may attempt an alternative analysis. From the non-dimensionalization of Section 6.1, we see that bulk modulus scales as $1/D^2$, where D is the object's largest diameter. Thus, if we assume that aggregates in space, though confined by pressures of less than 20 kPa, nevertheless display a plastic bulk modulus of 1 MPa, then for Brucemurray to be locally stable, it must be an object sized greater than 30 km. But such a large asteroid would have probably allowed estimates of its diameter. Alternatively, were Brucemurray less than a kilometer in extent, for it to be locally stable and have an internal friction angle of 30° would necessarily entail its κ to be less than 700 Pa; such a low modulus has to be confirmed by experiments on aggregates confined at around a kilometer sized Brucemurray's average internal pressure of 24 Pa. The only other possibilities are that Brucemurray rotates at a slower rate or has a greater ϕ_F.

We end this section by mentioning past work on the stability of granular asteroids. Holsapple (2004) too approached stability from an energetic viewpoint, but developed his stability test in terms of virtual displacements rather than in the rate form followed here. Interestingly though, while we couch our stability test as an extension of Pearson's (1955) restatement of the classical Lagrange–Dirichlet criterion, Holsapple (2004) framed his as an independent postulate. It will, therefore, be instructive to compare our predictions and highlight differences in our techniques.

Holsapple (2004) makes several assumptions that restrict his method's applicability. First, the derivation of the coordinate system in which stability is tested holds only for bodies that continue to rotate about a principal axis post-perturbation. Next, the contribution of the angular acceleration $\dot{\Omega}$ to relative kinetic energy is ignored, thereby restricting the stability test to principal-axes rotators that may be perturbed only in a manner that preserves angular momentum. The body's fate following perturbations that add angular momentum is unknown. Finally, perturbations are restricted to those that are compatible with the chosen plastic potential; cf. (33) and accompanying discussion. However, incompatible perturbations constitute an overwhelming majority; in the six-dimensional space of all possible strain perturbations of a material element, a compatible perturbation is just *one* choice.

If we restrict ourselves to angular momentum preserving compatible perturbations, we obtain results consistent with Holsapple (2004) as follows. For the case of inviscid incompressible fluids, where the yield surface collapses to a line, our stability predictions are identical as expected, because the only incompatible perturbations are those that do not preserve volume. Consider next solid objects that were modeled as elastic–plastic materials by Holsapple (2004), but as rigid-plastic materials here. When not critically equilibrated, such objects are predicted to be stable provided that their elastic moduli are high enough. We reach the same conclusion for the limiting case of a rigid-plastic ellipsoid. In our case, as a consequence of the maximum dissipation postulate, stability for rigid-plastic solids that are not critically equilibrated is decided at first-order itself, i.e., by $\delta^{(1)}E_k$'s sign in (30a). Furthermore, critically equilibrated elastic–plastic ellipsoids were predicted by Holsapple (2004) to become unstable to compatible perturbations in the presence of a small amount of material softening. Here, because a softening material has a non-convex yield

surface, the maximum dissipation postulate also predicts instability for rigid-plastic materials at first order itself; cf. Section 7.1.

To observe differences that may arise when we ignore incompatible perturbations and/or do not preserve angular momentum, consider the case of 1943 Anteros in Fig. 9 that for the sake of argument we take to be critically equilibrated. Given its shape and spin, the analysis here can predict Anteros' local response to *all* homogeneous perturbations. Perturbation that modify Anteros' angular momentum could potentially destabilize it. Anteros is stable, however, to incompatible perturbations that leave its angular momentum unchanged. For compatible angular momentum preserving perturbations that automatically do not affect the body's angular momentum, we are able to identify appropriate material parameters that would lead to instability. Now, as mentioned above, compatible perturbations constitute a one-dimensional subset of the six-dimensional space of displacement perturbations. Concluding that Anteros is stable on the basis of its response to a solitary perturbation may not be entirely justified, as it is entirely possible for Anteros to have during its lifetime seen perturbations that are incompatible.

Finally, there are differences also in the way granular aggregates are modeled. In contrast to us, Holsapple (2004) models rubble-piles as elastic–plastic materials, and this necessitated employing several parameters, obtained, in turn, from terrestrial soil tests conducted at confining pressures of several MPa. This ignored the fact that granular asteroids are confined by very low pressures, and this affects material properties; cf. Section 7.1. Our rigid-plastic constitutive description, on the other hand, requires only two parameters.

7.4. Planetary encounters

During a tidal flyby an asteroid experiences forces and torques over a finite duration. A rigorous investigation into the stability of asteroids to planetary encounters will, therefore, require that we follow the asteroid's dynamics during its flyby along, say, the lines of Sharma et al. (2006). Here, as a first step, we will approximate the flyby as a single instantaneous perturbation, and further assume that the asteroid's angular momentum is left unchanged by the tidal encounter; we comment on this latter assumption at the end of this section. The local secular stability results of the previous section then are satisfactory for small perturbations as experienced by an asteroid during a remote flyby. We now employ Section 6.5's analysis to investigate the stability of asteroids to close planetary encounters where the perturbations are potentially bigger.

After a close planetary flyby, asteroids that lie within the boundaries of their associated equilibrium region may suffer appreciable shape change, notwithstanding the first-order stability prediction of the maximum dissipation postulate. As an approximation we assume that, if $\delta^{(2)} E_k$ is positive for a choice of the ultimate friction angle ϕ_F and plastic bulk modulus κ, then the corresponding asteroid is unstable to a close flybys, else not. Fig. 11 locates the prolate near-Earth asteroids of Table 1 on Fig. 6, while also appending plots corresponding to a lower and a higher friction angle of, respectively, 20° and 50°. Fig. 12 repeats the process for the asteroids listed in Table 2 by locating them on Fig. 7 and on similar plots obtained for ϕ_F of 20° and 40°.

We have seen in the previous section that were Anteros considered critically equilibrated, for it to be locally stable, it requires a scaled plastic bulk modulus κ less than 10. From Fig. 11, we see that even if Anteros with a low internal pressure of 0.14 kPa had a higher friction angle ϕ_F of 50° – as suggested to be possible for lightly confined aggregates by experiments of Ponce and Bell (1971) discussed in Section 7.1 – for it to be stable to close flybys, it should not have a κ greater than 1. Obviously, given its location
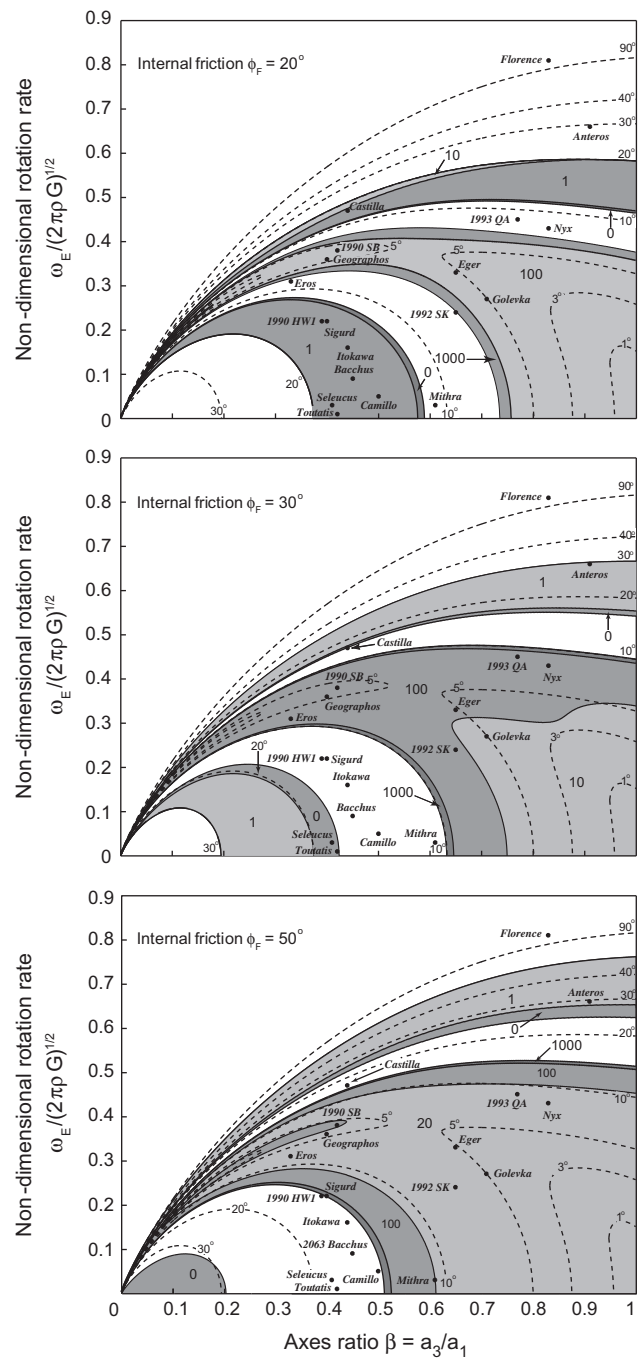

Fig. 11. Location of several prolate NEAs. See also Fig. 6's caption.

in shape–spin space, a ϕ_F below 30° is inadmissible for a noncohesive granular Anteros. Thus, both a local and an approximate higher-order stability analysis appear to indicate that for Anteros to be a rubble-pile asteroid it must have a very low plastic bulk modulus. If, in case, future experiments on soils at low-confinement pressures indicate that such low bulk modulus are unrealistic, then either Anteros is not a cohesionless granular aggregate, or it has never had a close tidal encounter as it is susceptible to significant reshaping. Exactly the same arguments may be made for Brucemurray and Nefertiti in Fig. 12.

Considering other asteroids in Fig. 11, we see that for 1990 SB, Geographos, Eger, Golevka, 1992 SK and Eros to be stable to close flybys, they must have a high plastic bulk modulus κ of at least 100 in case their friction angles are about 30°. At higher friction an-
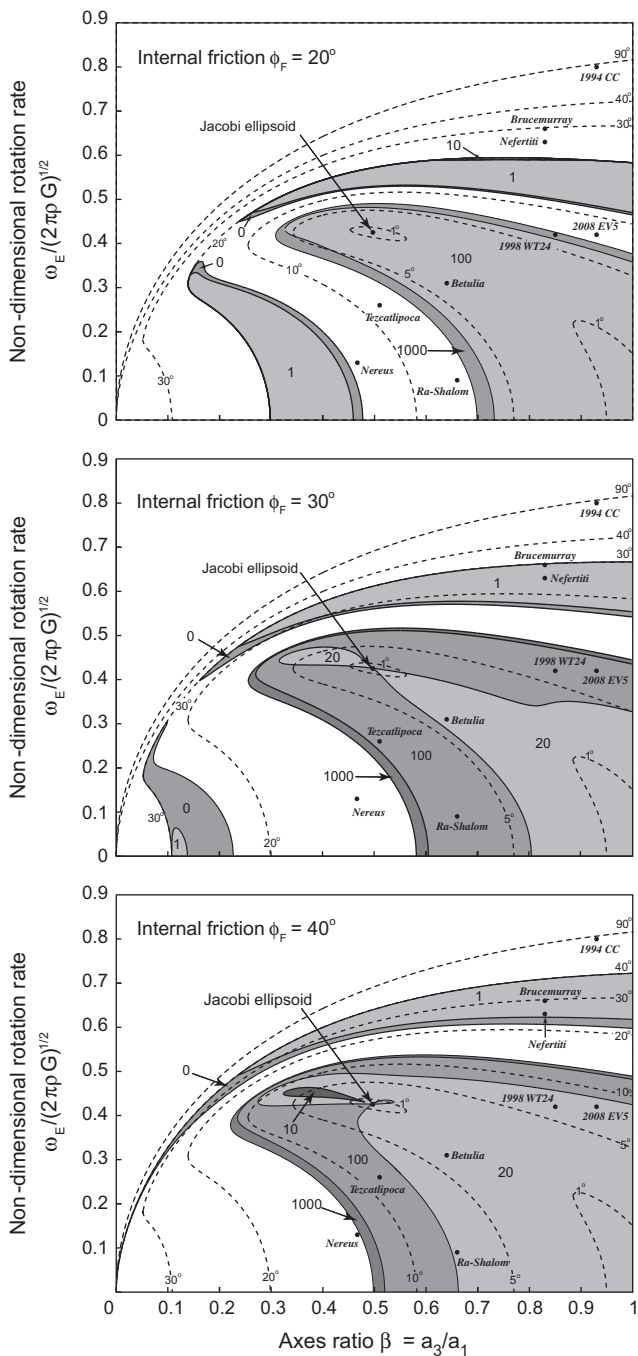
Fig. 12. Location of several average-triaxial NEAs. See also Fig. 6's caption.

gles, this lower bound on κ reduces to 20. For a 34 km Eros with a ϕ_F of 30°, this suggests a bulk modulus of at least 4 MPa. The average pressure within Eros is nearly 20 kPa, so that the bulk modulus' estimate correlates well with the experiments of Lancelot et al. (2006); cf. Section 7.1. On the other hand, Golevka is less than a kilometer in size, so that the mean internal pressure is a low 7 Pa, and a non-dimensional κ of 100 corresponds to about 1.2 kPa. It remains to be tested whether these are realistic estimates for the plastic bulk modulus. If not, then our conclusions will be as in the case of Anteros. Similar arguments hold for the triaxial asteroids in Fig. 12, except that a low friction angle of 20° appears less acceptable. We recall that all these asteroids, and also the ones discussed in the next paragraph, were already seen to be locally stable at first-order in Section 7.3, as they lie well within

equilibrium zones corresponding to any reasonable choice of the friction angle. Thus, even if they are found unstable to close planetary flybys, it does not prohibit their existence as granular aggregates.

We turn finally to the Itokawa and its neighbors 1991 HW, Sigurd, Bacchus, Camillo, Mithra, Seleucus and Toutatis in Fig. 11. We see from the plot corresponding to ϕ_F = 30° that, excepting the latter two, all the others will be unstable to a close flyby independent of κ's value. Seleucus and Toutatis lie just within a zone corresponding to zero plastic bulk modulus, and this κ appears unreasonable. Thus, in their case, if we require them to be stable to close encounters, they must have a friction angle less than 30° and a scaled κ of about 2. For the 4.6 km long Toutatis with average internal pressure of 0.4 kPa this gives a plastic bulk modulus of about 1.2 kPa. This again is a low value that needs experimental corroboration. Itokawa and the rest of its neighbors are stable to close tidal encounters only if either they have a friction angle of 20° and a κ of about 2, or a ϕ_F somewhat greater than 50° and a scaled plastic bulk modulus between 100 and 1000; cf. the top and bottom plots in Fig. 11. In case of the popular half-kilometer long Itokawa that has an internal mean pressure of a mere 5 Pa, these two cases correspond to bulk moduli of 15 Pa and 8 kPa, for internal friction angle choices of, respectively, 20° and 50°. The former estimate of κ appears unreasonably low, and we are inclined to believe that a granular Itokawa has a ϕ_F greater than 50° and a plastic bulk modulus around 10 kPa. It is interesting to note that modeling Itokawa as a contact binary Sharma (2009) found that a rubble-pile Itokawa requires an internal friction angle slightly beyond 50° to exist in equilibrium. Very similar arguments may be made for Nereus in Fig. 12.

Before closing this section we comment on our earlier decision to ignore the change in an asteroid's angular momentum during a planetary encounter. This holds strictly for asteroids having an axis of symmetry normal to the flyby plane, as tidal torques vanish. For other asteroids, there exist flyby parameters that ensure that the asteroid's angular momentum is affected little by a tidal flyby, see, e.g., Sharma et al. (2006). For the general case, if we were to admit perturbations that change an asteroid's angular momentum, then, as discussed in Section 5.2 and in Paper II, the present analysis would predict instability. This would be a rather crude first estimate, and for more accurate answers it will be necessary to extend the present analysis to include perturbations that occur over finite time during which angular momentum may be transferred.

8. Conclusion

In this paper, we have investigated the structural stability to infinitesimal perturbations of rubble-pile asteroids, modeling them as freely-rotating rigid-perfectly-plastic ellipsoids following an associative flow rule post-yield. To this end, we extended the classical Lagrange–Dirichlet theorem to the case of non-smooth materials like granular aggregates. We also discussed in detail the appropriate coordinate system in which to carry out the stability analysis; this was found to be the well-known Tisserand's mean axes of the body. We probed the stability of several near-Earth asteroids, and explored the influence of material parameters such as the ultimate internal friction angle ϕ_F and plastic bulk modulus κ. In this context, we also examined the stability of asteroids to planetary encounters after making several simplifying assumptions. Close encounters were investigated via an approximate stability analysis of finite perturbations. We saw that it may be possible for asteroids to be stable to small perturbations, but unstable to strong perturbations as experienced during close flybys. Conversely, assuming stability in certain situations, we could place bounds on the ϕ_F and κ of some asteroids. We saw that in

cases such as Anteros, stability could only be guaranteed if it had a κ lower than 10 kPa. The possibility of such a low modulus for soils needs to be verified experimentally by hydrostatic compression tests conducted at confining pressures of less than 100 Pa, as appropriate for kilometer sized granular asteroids.

In the future, we aim to apply the stability test developed here to the small newly-discovered moons of the giant planets, many of which are thought to be granular aggregates, and rubble-pile binaries. It is also necessary to extend the present analysis to include perturbations that are spread over finite time in order to address tidal flybys.

Acknowledgments

References

Benner, L.A.M. et al., 1997. Radar detection of near-Earth Asteroids 2062 Aten, 2101 Adonis, 3103 Eger, 4544 Xanthus, and 1992 QN. Icarus 130, 296–312.

Benner, L.A.M. et al., 1999. Radar observations of Asteroid 2063 Bacchus. Icarus 139, 309–327.

Blum, J., Schräpler, R., 2004. Structure and mechanical properties of high-porosity macroscopic agglomerates formed by random ballistic deposition. Phys. Rev. Lett. 93, 115503:1–115503:4.

Bolton, M.D., 2003. A Guide to Soil Mechanics, third ed. Universities Press, Hyderabad, India.

Brozovic, M. et al., 2010a. Radar observations and a physical model of Asteroid 4660 Nereus, a prime space mission target. Icarus 201, 153–166.

Brozovic, M. et al., 2011. Radar and optical observations and physical modeling of triple near-Earth Asteroid (136617) 1994 CC. Icarus 216, 241–256.

Brozovic, M., Benner, L.A.M., Magri, C., Ostro, S.J., Scheeres, D.J., Giorgini, J.D., Nolan, M.C., Margot, J.-L., Jurgens, R.F., Rose, R., 2010b. Radar observations and a physical model of contact binary Asteroid 4486 Mithra. Icarus 208, 207–220.

Burns, J.A., Safronov, V.S., 1973. Asteroid nutation angles. Mon. Not. R. Astron. Soc. 165, 403–411.

Busch, M.W. et al., 2008. Physical properties of near-Earth Asteroid (33342) 1998 WT24. Icarus 195, 614–621.

Busch, M.W. et al., 2011. Radar observations and the shape of near-Earth Asteroid 2008 EV5. Icarus 212, 649–660.

Busch, M.W., Ostro, S.J., Benner, L.A.M., Giorgini, J.D., Jurgens, R.F., Rose, R., Magri, C., Pravec, P., Scheeres, D.J., Broschart, S.B., 2006. Radar and optical observations and physical modeling of near-Earth Asteroid 10115 (1992 SK). Icarus 181, 145–155.

Chakrabarty, J., 1969. On uniqueness and stability in rigid/plastic solids. Int. J. Mech. Sci. 11 (9), 723–731.

Chandrasekhar, S., 1969. Ellipsoidal Figures of Equilibrium. Yale Univ. Press, New Haven, CT.

Chapman, C.R., Harris, A.W., Binzel, R.P., 1994. Physical properties of near-Earth asteroids: Implications for the hazard issue. In: Gehrels, T. (Ed.), Hazards Due to Comets & Asteroids. U. Arizona Press, Tucson, AZ, pp. 540–543.

Chen, W.F., Han, D.J., 1988. Plasticity for Structural Engineers. Springer-Verlag, New York.

Delbo, M., Harris, A.W., Binzel, R.P., Pravec, P., Davies, J.K., 2003. Keck observations of near-Earth asteroids in the thermal range. Icarus 166, 116–130.

Fujiwara, A. et al., 2006. The rubble-pile asteroid Itokawa as observed by Hayabusa. Science 312, 1330–1334.

Fukushima, S., Tatsuoka, F., 1984. Strength and deformation characteristics of saturated sand at extremely low pressures. Soils Found. 24, 30–48.

Greenwood, D.T., 1988. Principles of Dynamics. Prentice-Hall, Englewood Cliffs, NJ.

Harris, A.W., Fahnestock, E.G., Pravec, P., 2009. On the shapes and spins of "rubble pile" asteroids. Icarus 199, 310–318.

Hill, R., 1957. Stability of rigid/plastic solids. J. Mech. Phys. Solids 6 (1), 1–8.

Holsapple, K.A., 2001. Equilibrium configurations of solid cohesionless bodies. Icarus 154, 432–448.

Holsapple, K.A., 2004. Equilibrium figures of spinning bodies with self-gravity. Icarus 172, 272–303.

Holsapple, K.A., 2007. Spin limits of Solar System bodies: From the small fast-rotators to 2003 EL61. Icarus 187, 500–509.

Holzapfel, G.A., 2001. Nonlinear Solid Mechanics. John Wiley and Sons, New York.

Hudson, R.S. et al., 2000. Radar observations and physical model of Asteroid 6489 Golevka. Icarus 148, 37–51.

Hudson, R.S., Ostro, S.J., 1994. Shape of Asteroid 4769 Castalia (1989 PB) from inversion of radar images. Science 263, 940–943.

Hudson, R.S., Ostro, S.J., 1995. Shape and non-principal axis spin state of Asteroid 4179 Toutatis. Science 270, 84–86.

Hudson, R.S., Ostro, S.J., 1999. Physical model of Asteroid 1620 Geographos from radar and optical data. Icarus 140, 369–378.

Jaeger, H.M., Nagel, S.R., 1992. The physics of the granular state. Science 255, 1523–1531.

Jeans, J.H., 1961. Astronomy and Cosmogony, second ed. Dover, New York.

Jenkins, J.T., Zhang, C., 2002. Kinetic theory for nearly elastic, slightly frictional spheres. Phys. Fluids 14, 1228–1235.

Kaasalainen, M. et al., 2004. Photometry and models of eight near-Earth asteroids. Icarus 167, 178–196.

Lade, P.V., Yamamuro, J.A., Liggio Jr., C.D., 2009. Effects of fines content on void ratio, compressibility, and static liquefaction of silty sand. Geomech. Eng. 1, 1–15.

Lancelot, L., Shahrour, I., Mahmoud, M.A., 2006. Failure and dilatancy properties of sand at relatively low stresses. J. Eng. Mech. ASCE 132, 1396–1399.

LaSalle, J., Lefschetz, S., 1961. Stability by Lyapunov's Direct Method. Academic Press, New York.

Lubarda, V., 1999. Viscoplasticity Theory. CRC, New York.

Lubliner, J., 1990. Plasticity Theory. Macmillan, New York.

Lyttleton, R.A., 1953. The Stability of Rotating Liquid Masses. Cambridge U. Press, Cambridge.

Magri, C. et al., 2011. Radar and photometric observations and shape modeling of contact binary near-Earth Asteroid (8567) 1996 HW1. Icarus 214, 210–227.

Magri, C., Ostro, S.J., Scheeres, D.J., Nolan, M.C., Giorgini, J.D., Benner, L.A.M., Margot, J.-L., 2007. Radar observations and a physical model of Asteroid 1580 Betulia. Icarus 186, 152–177.

Munk, W., MacDonald, G., 1960. The Rotation of the Earth. Cambridge U. Press, Cambridge.

Nguyen, Q.S., 2000. Stability and Nonlinear Solid Mechanics. John Wiley & Sons, New York.

Pearson, C.E., 1955. General theory of elastic stability. Q. Appl. Math. 14 (2), 133–144.

Ponce, V.M., Bell, J.M., 1971. Shear strength of sand at extremely low pressures. J. Geotech. Eng. ASCE (J. Soil Mech. Found. Div. ASCE) 97, 625–638.

Pravec, P., Wolf, M., Šarounová, L., 1998. Lightcurves of 26 near-Earth asteroids. Icarus 136, 124–153.

Richardson, D.C., Elankumaran, P., Sanderson, R.E., 2005. Numerical experiments with rubble piles: Equilibrium shapes and spins. Icarus 173, 349–361.

Rosenkilde, C.E., 1967. The tensor virial-theorem including viscous stress and the oscillations of a Maclaurin spheroid. Astrophys. J. 148, 825–841.

Sanchez, P., Scheeres, D.J., 2011. Simulating asteroid rubble piles with a self-gravitating soft-sphere distinct element method model. Astrophys. J. 727, 120–133.

Sanchez, P., Scheeres, D.J., 2012. DEM simulation of rotation-induced reshaping and disruption of rubble-pile asteroids. Icarus 218, 876–894.

Scheeres, D.J., Hartzell, C.M., Sanchez, P., Swift, M., 2010. Scaling forces to asteroid surface: The role of cohesion. Icarus 210, 968–984.

Sharma, I., 2004. Rotational Dynamics of Deformable Ellipsoids with Applications to Asteroids. Ph.D. Thesis, Cornell University.

Sharma, I., 2009. The equilibrium of rubble-pile satellites: The Darwin and Roche ellipsoids for gravitationally held granular aggregates. Icarus 200, 636–654.

Sharma, I., 2010. Equilibrium shapes of rubble-pile binaries: The Darwin ellipsoids for gravitationally held granular aggregates. Icarus 205, 638–657.

Sharma, I., 2012. Stability of rotating non-smooth complex fluids. J. Fluid Mech. 708, 71–99.

Sharma, I., Burns, J.A., Hui, C.-Y., 2005. Nutational damping times in solids of revolution. Mon. Not. R. Astron. Soc. 359, 79–92.

Sharma, I., Jenkins, J.T., Burns, J.A., 2005. Equilibrium shapes of ellipsoidal soil asteroids. In: García-Rojo, R., Hermann, H.J., McNamara, S. (Eds.), Proceedings of the 5th International Conference on Micromechanics of Granular Media, vol. 1. A.A. Balkema, pp. 429–432.

Sharma, I., Jenkins, J.T., Burns, J.A., 2006. Tidal encounters of ellipsoidal granular asteroids with planets. Icarus 183, 312–330.

Sharma, I., Jenkins, J.T., Burns, J.A., 2009. Dynamical passage to approximate equilibrium shapes for spinning, gravitating rubble asteroids. Icarus 200, 304–322.

Shepard, M.K. et al., 2008. Multi-wavelength observations of Asteroid 2100 Ra-Shalom. Icarus 193, 20–38.

Storåkers, B., 1977. On uniqueness and stability under configuration-dependent loading of solids with or without a natural time. J. Mech. Phys. Solids 25 (4), 269–287.

Sture, S., Batiste, S.N., AlShibli, K.A., Swanson, R.A., 1998. Mechanics of granular materials at low effective pressures. J. Aerospace Eng. ASCE 11, 67–72.

Veverka, J. et al., 2000. NEAR at Eros: Imaging and spectral results. Science 289, 2088–2097.

Vilas, F., Tholen, D.J., Lebofsky, L.A., Campins, H., Veeder, G.J., Binzel, R.P., Tokunaga, A.T., 1985. Physical parameters of near-Earth Asteroid 1982 DV. Icarus 63, 201–205.

Ziegler, H., 1968. Principles of Structural Stability. Blaisdell Pub. Co., Waltham, MA.